JOURNAL OF GEOPHYSICAL RESEARCH, VOL. 110, D24311, doi:10.1029/2005JD006318, 2005

Retrieval of biomass combustion rates and totals from fire radiative power observations:
FRP derivation and calibration relationships between biomass consumption and fire radiative energy release

M. J. Wooster, G. Roberts, and G. L. W. Perry[1]
Department of Geography, King's College London, Strand, London, UK

Y. J. Kaufman
Laboratory for Atmospheres, NASA Goddard Space Flight Center, Greenbelt, Maryland, USA

Received 2 June 2005; revised 22 September 2005; accepted 20 October 2005; published 31 December 2005.

[1] Estimates of wildfire aerosol and trace gas emissions are most commonly derived from assessments of biomass combusted. The radiative component of the energy liberated by burning fuel can be measured by remote sensing, and spaceborne fire radiative energy (FRE) measures can potentially provide detailed information on the amount and rate of biomass consumption over large areas. To implement the approach, spaceborne sensors must be able to derive fire radiative power (FRP) estimates from subpixel fires using observations in just one or two spectral channels, and calibration relationships between radiated energy and fuel consumption must be developed and validated. This paper presents results from a sensitivity analysis and from experimental fires conducted to investigate these issues. Within their methodological limits, the experimental work shows that FRP assessments made via independent hyperspectral and MIR radiance approaches in fact show good agreement, and fires are calculated to radiate 14 ± 3% [mean ± 1S.D.] of their theoretically available heat yield in a form capable of direct assessment by a nadir-viewing MIR imager. The relationship between FRE and fuel mass combusted is linear and highly significant ($r^2 = 0.98$, $n = 29$, $p < 0.0001$), and FRP is well related to combustion rate ($r^2 = 0.90$, $n = 178$, $p < 0.0001$), though radiation from the still-hot fuel bed can sometimes contribute significant FRP from areas where combustion has ceased. We conclude that FRE assessment offers a powerful tool for supplementing existing burned-area based fuel consumption measures, and thus shows significant promise for enhancing pyrogenic trace gas and aerosol emissions estimates.

Citation: Wooster, M. J., G. Roberts, G. L. W. Perry, and Y. J. Kaufman (2005), Retrieval of biomass combustion rates and totals from fire radiative power observations: FRP derivation and calibration relationships between biomass consumption and fire radiative energy release, *J. Geophys. Res.*, *110*, D24311, doi:10.1029/2005JD006318.

1. Introduction

[2] Trace gases and particulates released during anthropogenic and naturally-occurring biomass burning have globally significant influences on Earth's atmosphere and radiation budget, but as yet these are incompletely understood and in some cases poorly quantified. In particular, many of the emitted trace gases have oxidising, acidifying and infrared-absorbing characteristics, while the organic carbon and black carbon aerosols respectively scatter and absorb solar radiation and can significantly influence cloud characteristics [*Rosenfeld*, 1999; *Andreae and Merlet*, 2001; *Chou et al.*, 2002; *Kaufman et al.*, 2002]. The influence of biomass burning on atmospheric chemistry, climate radiative forcing and precipitation is, therefore, a complex issue of scientific importance, and due to the rapidly varying, wide ranging nature of wildfires, any analysis of their large-scale effects generally necessitates the use of satellite-derived data sets [*Menzel and Prins*, 1996; *Scholes and Andreae*, 2000; *Kaufman et al.*, 2002].

[3] Within the last 5–10 years, new satellite-based instrumentation has been used to directly investigate the atmospheric distribution of specific biomass burning aerosols and trace gases; *Borrell et al.* [2001] and *Kaufman et al.* [2002] provide summary reviews of these applications. The sensors and methods used to perform such studies are continuing to rapidly advance [e.g., *King et al.*, 1999; *Borrell et al.*, 2003], but only certain compounds can be investigated in this way and in many cases retrieval methods are still being optimised. Currently, therefore, most

---

[1] Also at School of Geography and Environmental Science, University of Auckland, Auckland, New Zealand.

0148-0227/05/2005JD006318

pyrogenic trace gas and aerosol emissions estimates are derived by applying so-called 'emissions factors' (typically expressed as grams of species emitted per kg of dry fuel burned [*Andreae and Merlet*, 2001]) to assessments of the amount of fuel biomass combusted, this typically obtained via remote sensing of burned area [e.g., *Ito and Penner*, 2004; *Korontzi et al.*, 2004], and the formula first suggested by *Seiler and Crutzen* [1980]:

$$M = A\beta\rho \qquad (1)$$

where M is the estimated fuel mass combusted (kg), A is burned area (m^2), β is fuel density (kg/m^2), and ρ is the combustion completeness (the fraction of the available fuel that is actually burnt).

[4] The accuracy of regional to global scale burned area (A) measures is rapidly improving due to superior remote sensing data sets [e.g., *Zhang et al.*, 2003; *Korontzi et al.*, 2004], new algorithm enhancements [e.g., *Roy et al.*, 2002; *Stroppiana et al.*, 2003], and better resources to access and process long time-series [e.g., *Barbosa et al.*, 1999]. Nevertheless, significant uncertainly still remains. For example, *Korontzi et al.* [2004] obtained fuel consumption estimates for southern Africa that varied by a factor of four when parameterised with different EO-derived burned area products. Spatial and temporal information on the parameters β and ρ is considerably more difficult to obtain over large scales than is burned area [*French et al.*, 2004; *GTOS*, 2000], and no reliable EO-based method to accurately quantify these has been demonstrated thus far. Based on rigorous syntheses of past studies, many of which utilised an approach based on equation (1), the uncertainty in mean global fuel consumption is believed to be at least ±50% [*Andreae and Merlet*, 2001], and maybe much larger for individual environments or fire events. Arguably there appears to be no immediate opportunity for dramatically improving parameterisation of equation (1) through new EO-based estimates of β and ρ, and this has led to calls for new EO-based approaches to more directly assess pyrogenic fuel consumption [*Andreae and Merlet*, 2001; *French et al.*, 2004]. One candidate approach is via assessment of the fire-emitted energy, since this should be a direct function of the fuel biomass combusted [*Wooster et al.*, 2004].

[5] For many years ecologists have used in situ measurements of fuel heat yield, biomass consumption per unit area and fire rate of spread to calculate fireline intensity (FLI), a measure of the total rate of heat release from the fire (generally expressed per unit length of the fire front [*Byram*, 1959; *Alexander*, 1982; *Whelan*, 1995]). The radiant component of this energy release (the so-called 'fire radiative power', FRP) has been demonstrably measured via airborne infrared radiometry [*Kaufman et al.*, 1996; *Riggan et al.*, 2004] and it is also possible to quantify this parameter using just the few IR channels typically available on satellite-borne imaging radiometers [*Kaufman et al.*, 1998a, 1998b; *Wooster et al.*, 2003]. Spaceborne FRP observations have already been used to investigate significant spatio-temporal differences in fire radiative intensity [e.g., *Wooster and Zhang*, 2004; *Smith and Wooster*, 2005], and provided a consistent relationship can be demonstrated between the radiant energy release and the fuel biomass consumed in a fire, then in future EO-based biomass combustion estimates can potentially be derived via temporal integration of spaceborne FRP retrievals. This paper investigates relationships between radiative energy emission and fuel consumption, deriving FRP via both hyperspectral and single-waveband algorithms. The latter method is based on observations made by a middle infrared (MIR) imaging system whose spectral sensitivity is well-matched to that of key spaceborne MIR detectors such as those of EOS-MODIS, and its sensitivity to the algorithm assumptions and potential parameterisation error is assessed herein. A companion paper [*Roberts et al.*, 2005] validates and intercompares FRP derived using data from different spaceborne sensors, and uses MODIS and geostationary Metosat-8 Spinning Enhanced Visible and Infrared Imager (SEVIRI) imagery of southern Africa to provide the first FRP-derived semi-continental scale combustion rate and total fuel consumption estimates for this region, which is responsible for between one-fifteenth and one-fifth of global wildfire emissions [*Andreae*, 1991; *Scholes et al.*, 1996].

2. Vegetation Combustion and Fire Radiative Power

[6] Vegetation consists of a number of fuel components (e.g., live foliage, dead leaf litter and woody materials). Each contains energy stores in a variety of chemical forms (cellulose, hemicelluloses, lignin, proteins, nucleic acids, amino acids, and volatile extractives [*Whelan*, 1995]) but the total amount of energy released per unit mass of dry fuel fully burned is surprisingly consistent across vegetation types at between 16 000 and 22 000 $kJ.kg^{-1}$ [*Lobert and Warnatz*, 1993; *Whelan*, 1995; *Trollope et al.*, 1996]. These values are also large, though actual heat releases in natural wildfires are generally somewhat less than the laboratory-determined theoretical maximum, due for example to the effects of incomplete combustion [*Pyne*, 1984; *Alexander*, 1982; *McNaughton et al.*, 1998; *Smith et al.*, 2005]. A significant proportion of this energy is lost by processes other than radiation (e.g., convection, conduction, and vaporisation), but nevertheless wildfire radiative power emissions are intense and very suitable for assessment via satellite Earth observation.

[7] In order to use FRP measures to quantify wildfire biomass consumption, the relationship between these two parameters must be derived. *Wooster* [2002] demonstrated a linear relationship between fuel consumption and total emitted fire radiative energy (FRE; the temporal integral of FRP) but, in addition to the relatively small sample size (n = 12), a number of other factors limit the applicability of that study to the satellite remote sensing situation. First, *Wooster* [2002] retrieved FRE via hyper-spectral observations in the 0.4–2.5 μm wavelength region. However, the moderate-to-low spatial resolution spaceborne systems used for active fire detection and characterisation typically have only a few spectral channels, and a spatial resolution that means that any active fire 'signal' is usually not detectable in this visible-to-shortwave infrared spectral interval. Rather, fire detection from space using systems such as the BIRD-HSRS, EOS-MODIS, and GOES Imager [*Zhukov et al.*, 2005a; *Justice et al.*, 2002; *Prins et al.*, 1998] (respectively) usually requires observations in the middle

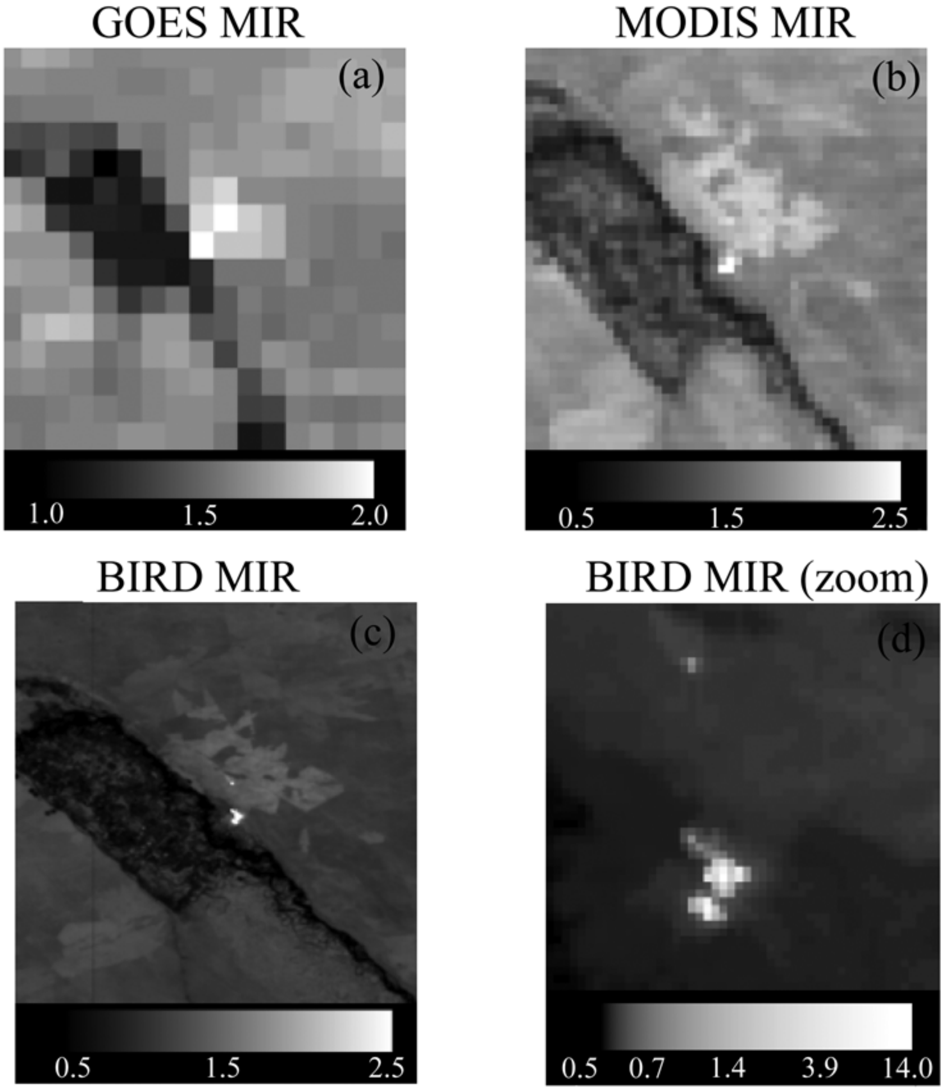

Figure 1. Imagery from the middle infrared channels of the GOES-8 Imager, EOS MODIS and BIRD HSRS sensors, showing the MIR spectral radiance ($W/m^2/sr/\mu m$) of a fire burning alongside the Rio Negro river in Argentina on 14 January 2003 (14:30 GMT ± 30 min). Fire-affected pixels are easily discriminated by their elevated radiance, despite the active fire front being a significantly subpixel phenomena. The MIR fire pixel radiances recorded by BIRD HSRS are significantly higher than those recorded by the other sensors due to its higher (370 m) spatial resolution compared to MODIS (1 km) and GOES (4 km), the active fire therefore forming a larger proportion of the pixel.

infrared (MIR) region (e.g., Figure 1) since the fires radiant intensity is greatest in this spectral window. In this case, reliable detection of pixels containing actively burning fires can occur even when the fire is very small compared to the sensor spatial resolution, down to fires covering around 10^{-3} to 10^{-4} of the pixel area, depending on the relative dominance of lower temperature smoldering or higher temperature flaming activity [*Robinson*, 1991]. As such, even the rather coarse spatial resolution data available from geostationary platforms can be successfully used to detect active fires, as the successful Automated Biomass Burning Algorithm (ABBA [*Prins and Menzel*, 1994]) and its successor, the Wildfire ABBA [*Prins et al.*, 1998], clearly demonstrate. However, as Figure 1 shows, as spatial resolution decreases the spatial detail is reduced and the spectral radiance contrast between fire pixels and surrounding non-fire pixels decreases (since the fire typically covers a smaller fraction of the pixel area). This essentially makes fires of a given size more difficult to detect as spatial resolution decreases, and causes a certain proportion of the smallest or most weakly burning fires to be missed altogether. Despite such limitations, the geostationary systems offer the potentially great advantage that, cloud cover permitting, they can record the complete FRP lifecycle of a fire, and thus can be used to derive direct measures of FRE via temporal integration of the FRP observations. *Wooster et al.* [2004] first indicated this possibility with GOES data of an Alaskan fire, while the companion work to the current paper [*Roberts et al.*, 2005] demonstrates this fully using data from Meteosat-8 SEVIRI.

[8] To be fully applicable to spaceborne EO data, retrievals of FRP used to derive ‘combustion factor’ relationships between fire radiative energy emissions and fuel consumption should be conducted using a MIR-based method, since it is this single waveband approach that is most appropriate for use with geostationary and other lower spatial resolution spaceborne data [*Wooster et al.*, 2003]. Ideally FRE estimates derived in this way should be compared to those made via multi-spectral approaches, allowing the sensitivity of retrieval to the spectral interval and method used to be examined [*Giglio and Justice*, 2003]. Furthermore, as already stated, satellite EO provides instantaneous measures of FRP, rather than direct estimates of total FRE, and so the relationship between FRP and rate of fuel combustion, rather than simply their time-integrated totals, should also be examined.

[9] Based on fieldwork conducted in the summer of 2003, this paper reports the results of experiments designed to (1) validate the MIR radiance method of FRP derivation, via comparison to an alternative hyperspectral approach previously used to estimate energy emissions from active lava having a temperature distribution similar to that of vegetation fires [*Flynn et al.*, 1993], and (2) derive a calibration relationship between the rates and totals of fire radiative energy release and fuel consumption. The experiments used observation conditions more akin to those found when studying fires from airborne or spaceborne platforms than was the case in *Wooster* [2002]; namely, outdoor fires viewed at zenith angles at or close to nadir, mixtures of herbaceous and woody fuels, fuel mass totals varying over two orders of magnitude, and a fuel bed sufficiently large to sustain a moving flame front.

3. Remote Sensing Fire Radiative Power

[10] The temperatures of active fires vary widely, with *Ohlemiller* [1995] suggesting 675 K as the lower temperature limit of smoldering wood, and *Riggan et al.* [2004] suggesting temperatures in the flaming zone of up to perhaps 1600 K. A single wildfire is likely to consist of multiple flaming and smoldering zones, with a range of temperatures fluctuating at small spatial scales. The FRP of such a fire (here expressed per unit area of the ground-field of view) is given by the Stefan-Boltzmann law, which can be adapted to the multi-thermal component situation as:

$$FRP_{TRUE} = \varepsilon\sigma \sum_{k=1}^{n} p_k T_k^4 \qquad \left[\mathrm{Wm}^{-2}\right] \tag{2}$$

where $\mathrm{FRE_{TRUE}}$ = Fire Radiative Power (Wm^{-2}), n = number of temperature components in the fire, σ = Stefan-Boltzmann constant (5.67×10^{-8} J s^{-1} m^{-2} K^{-4}), ε = fire graybody emissivity, p_k = fractional area of kth surface thermal component within the field of view, and T_k = kinetic temperature of the kth thermal component (K).

[11] However, equation (2) can only be used to calculate FRP from remotely sensed measurements if the radiative temperatures of the individual fire components vary over spatial scales capable of being resolved by the instrument (which can be $\sim$ millimetres [*Gaydon and Wolfhard*, 1970]). Furthermore, when observing from space, the fire as a whole is generally much smaller than a pixel (i.e. $\sum_{k=1}^{n} p_k \ll 1$), such that the fire pixel’s radiative brightness temperature can be very significantly lower than the fire’s true radiative temperature. For these reasons alternative methods of FRP derivation are required for subpixel fires.

3.1. FRP Retrieval via the Bi-Spectral Method

[12] One approach employed to retrieve FRP from subpixel fires is *Dozier*’s [1981] bi-spectral method, which uses the fire pixel signal in two widely-separated infrared channels (usually MIR and TIR) to retrieve the temperature (T_f) and fractional area (P_f) of a theoretically homogeneous (i.e., single temperature) fire that would provide the observed two channel signal. An estimate of FRP can then be made via use of T_f and p_f in (2), the adapted Stefan-Boltzmann law. *Wooster et al.* [2003] and *Zhukov et al.* [2005b] discuss the bi-spectral approach and its routine application to data from the BIRD HSRS instrument, and it is also used as part of GOES ABBA Product generation [e.g., *Menzel and Prins*, 1996]. Since it uses the contribution of the fire to the pixel signal in two spectral bands, the *Dozier* [1981] bi-spectral method is sensitive to any interchannel FOV spatial misregistration or point spread function (PSF) differences [*Langaas*, 1993]. This can cause, for example, the radiant power contribution from a fire to vary between the spectral bands of the sensor, with the result that the fire may contribute proportionally more to the MIR band signal of a ‘fire’ pixel than to the TIR band for example (with the reverse likely in the neighbouring pixel). Such effects invalidate the bi-spectral model’s assumption that the fire fractional area is consistent across the MIR and TIR spectral bands of the fire pixel, and thus perturb the retrieval of fire fractional area and temperature [*Oertel et al.*, 2003; *Zhukov et al.*, 2005a, 2005b]. However, careful application of the bi-spectral approach can mitigate the consequences of interchannel spatial misregistration and PSF differences, generally by analysing the cumulative signal of clusters of spatially contiguous fire pixels rather than the individual fire pixels themselves [*Zhukov et al.*, 2005b].

[13] The bi-spectral approach is generally considered the most suitable FRP approach for use with data from higher spatial resolution imagers, such as airborne scanners [e.g., *Riggan et al.*, 2004] or the Hot Spot Recognition Sensor onboard the Bi-Spectral Infrared Detection (BIRD) Small Satellite Mission [*Zhukov et al.*, 2005a, 2005b]. However, when used with lower spatial resolution imagery, a second source of potential error can become very significant during application of the bi-spectral method. This is the uncertainty in quantifying the radiance from the ambient background part of the fire pixel or fire pixel cluster, which the bi-spectral approach requires to solve the dual waveband equations that consider the fire pixel as a homogenous subpixel fire superimposed on a homogenous ambient background [*Dozier*, 1981; *Robinson*, 1991]. Quantification of the ambient background radiance is generally retrieved via analysis of neighbouring nonfire pixels, but differences in altitude, land cover type and the proportion of solar-heated or still-cooling fire scars can make the signal of these surrounding nonfire pixels somewhat different to that of the ambient background part of the fire pixel itself. Indeed the surrounding nonfire pixels are themselves likely to vary somewhat in their spectral radiance signal due to such effects, and the resultant uncertainly in the chosen back-

ground pixel radiance value is often denoted by the standard deviation of the signal from the N background pixels considered [*Zhukov et al.*, 2005a, 2005b]. Provided the fire covers a sufficiently large fraction of the pixel area however, such uncertainty in the ambient background signal is relatively unimportant since the radiance contribution from the fire dominates the overall fire pixel radiance. However, for lower spatial resolution sensors this may not always be the case, most particularly in the TIR band where for the smaller or more weakly burning fires the fire pixel signal can be little different from the signal level of the ambient background pixels. As an example, consider a fire of temperature 800 K and fractional area 0.001, superimposed on a 300 K background. Without consideration of atmospheric and emissivity effects, the fire raises the MIR pixel brightness temperature by more than 30 K compared to the neighbouring nonfire background pixels, but concurrently raises the TIR channel brightness temperature by less than 1.5 K. Expanding the fire pixel fraction to 0.005 increases these values to 75 and 6 K respectively, and given the expected level of variation in the background pixel brightness temperatures/radiances, it can be seen that the precise effect of the sub pixel fire is likely to be much more easily quantified in the MIR spectral channel rather than in the TIR. This greatly diverging effect of sub pixel fires on the MIR and TIR channel fire pixel signal is exactly what makes the MIR-TIR brightness temperature difference such a sensitive fire pixel detection measure [*Robinson*, 1991; *Menzel and Prins*, 1996; *Kaufman et al.*, 1998a]. Since with lower spatial resolution sensors the fire pixel signal increase in the TIR channel signal can quite often be of a similar magnitude to the temperature variation between the surrounding ambient background pixels, and in some cases is small enough to be unduly influenced by sensor noise [*Giglio and Kendall*, 2001; *Wooster et al.*, 2003], very large uncertainties in the retrieval of fire temperature, fractional area, and FRP can result from application of the bi-spectral method in such situations. *Giglio and Kendall* [2001] performed a comprehensive sensitivity analysis of the bi-spectral approach, indicating its strengths but also showing that it may be considered properly appropriate only for fires whose fractional area within a pixel exceeds at least 0.005.

3.2. FRP Retrieval via Single Waveband Methods

[14] Because of the limitations of the bi-spectral method, most particularly its sensitivity to uncertainty in the TIR background characterisation and TIR channel noise, alternative methods for deriving FRP have been considered that rely only on isolating the fires signal in the MIR spectral region, where it is most intense. The first such method was that of *Kaufman et al.* [1996, 1998a, 1998b] for use with MODIS, empirically relating FRP directly to the brightness temperature of the MIR 'fire' pixel:

$$FRP_{MODIS} = 4.34.10^{-19}\left(T_{MIR}^{8} - T_{b,MIR}^{8}\right) \qquad \left[\mathrm{Wm}^{-2}\right] \quad (3)$$

where T_{MIR} and $T_{MIR,b}$ are, respectively, the radiative brightness temperatures of the fire pixel and the neighbouring nonfire background (K) recoded in the MODIS MIR channel.

[15] A major advantage of equation (3) is that it relies only on quantification of the fire pixel in a single spectral channel, removing problems related to interchannel spatial mis-registration. Furthermore, because it uses the MIR spectral band, where the signal from the fire is at a maximum, the effect of uncertainty in the ambient background signal is lessened when compared to situations where quantification of the TIR signal is also required [*Giglio and Kendall*, 2001; *Wooster et al.*, 2003]. FRP estimates provided via this 'MODIS method', are a key parameter in the MODIS Fire Product suite [*Justice et al.*, 2002].

[16] An alternative single waveband approach to FRP derivation is the MIR radiance method, first presented by *Wooster et al.* [2003] and based on simple approximations to the physical laws governing the emission of thermal radiation from fires. Like the MODIS method, the approach relies on quantification of the fire pixel and ambient background pixel signals in only the MIR spectral band, and so exhibits the two advantages cited above for the MODIS method. The main algorithmic difference is that in the MIR radiance method signals are quantified in terms of pixel spectral radiance rather than brightness temperature, and the equation is linear. This allows perturbations, due to atmospheric correction and varying pixel area across the swath for example, to be accounted for after initial FRP derivation if necessary. The primary assumption in the MIR radiance method is that Plank's Radiation law $B(\lambda, T)$ governing the relationship between emitted spectral radiance and emitter temperature (T) is well approximated by a fourth order power law for wavelengths in the MIR atmospheric window (3.4–4.2 μm) and the temperatures predominating in active fires (Figure 2a). In this way, the MIR emitted spectral radiance of a fire, $L_{f,MIR}$, can be approximated by:

$$L_{f,MIR} = \varepsilon_{f,MIR}B(\lambda, T) \approx \varepsilon_{f,MIR}aT^{4} \quad (4)$$

where $\varepsilon_{f,MIR}$ is the emissivity of the fire in the MIR spectral band, a is a constant with units W m^{-4} sr^{-1} m^{-1} K^{-4} (whose value is governed by the exact wavelength λ and fire temperature range over which the approximation is made). This power law relation is identical in form to the Stefan-Boltzmann law (Radiative Power = $\varepsilon\sigma T^4$), and equating these two relations allows the dependence upon emitter temperature (T) to be removed and the true fire thermal emission over all wavelengths (i.e., the fire radiative power) to be estimated directly from the fire-emitted MIR spectral radiance, without knowledge of the fire temperature (or, assuming in reality that the fire has more than one thermal component, the fire temperature distribution):

$$FRP_{MIR} = \left(\frac{\sigma.\varepsilon_{f}}{a.\varepsilon_{f,MIR}}\right)L_{f,MIR} \qquad \left[\mathrm{Wm}^{-2}\right] \quad (5)$$

where σ is the Stefan-Boltzmann constant (5.67×10^{-8} W m^{-2} K^{-4}), ε_f is the emissivity of the fire over all wavelengths and ε_{MIR} is the emissivity over the MIR spectral band. In the absence of data to the contrary gray body behaviour is assumed ($\varepsilon_f = \varepsilon_{f,MIR}$), and this is understood to be a realistic approximation for vegetation fires [*Langaas*, 1995]. $L_{f,MIR}$ (Wm^{-2} sr^{-1} μm^{-1}) is the fire-emitted spectral radiance, which in a similar way as for the bi-spectral method is generally calculated as the difference between the MIR spectral radiance of the active fire pixel

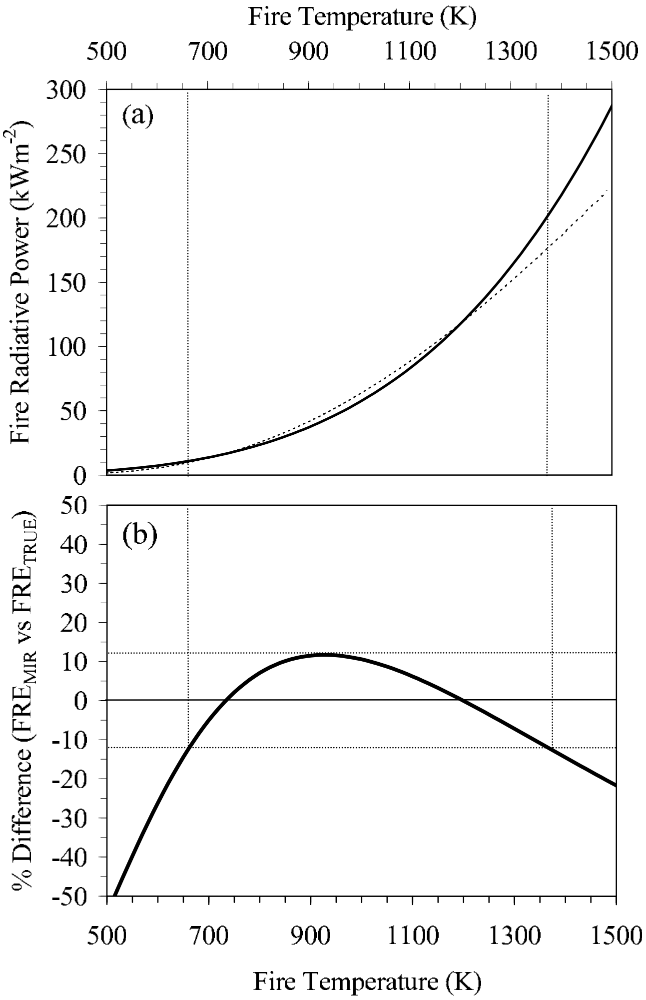

Figure 2. Fire Radiative Power derivation. (a) FRP_{TRUE} derived via the Stefan-Boltzmann law (solid line; equation (2)) and its approximation derived via the MIR radiance method (dashed line; equation (5) [*Wooster et al.*, 2003]) for a 500–1500 K fire temperature range. (b) Percentage difference between these two measures. Horizontal lines in Figure 2b denote ± 12% accuracy limits of the MIR radiance method, lying within the temperature range 665–1365 K (vertical lines). Calculations here assume fire fills the pixel.

and that of surrounding nonfire 'background' pixels (see the full derivation of equation (10) below).

[17] Details of the derivation of equation (5), and of its accuracy with respect to the bi-spectral and MODIS methods was previously provided by *Wooster et al.* [2003]. A key advantage of the technique is that it avoids the need to quantify the fire signal in the TIR spectral band, where variance in the background pixel radiances can be of a similar magnitude to the fire pixel radiance elevation itself. However, a major assumption during the derivation of equation (5) is the necessity to use a fourth order power law approximation to Planck's radiation law, since the soundness of this approximation varies somewhat over the temperature range considered appropriate to active fires (i.e. $\sim$600 K < T_f < 1600 K), and breaks down markedly outside this range. Figure 2b shows the degree of departure between the true fire radiative power, calculated via equation (2), and the MIR radiance method calculated via equation (5), assuming the pixel is filled by fire, the fire is a blackbody, and atmospheric effects are negligible. This represents an idealised case, most closely matched when viewing relatively thick flames with a MIR sensor placed at close range. Such a scheme is broadly consistent with the ground-based experiment described in section 4, and in this case FRP_{MIR} lies within ±12% of FRP_{TRUE} for T_f between 665 K and 1365 K. The fact that in real fires a mixture of temperatures exists at the subpixel scale will tend to improve accuracy further, since the FRP underestimation inherent towards the upper and lower temperature limits will be to some extent counteracted by overestimation from the mid-range emitters. *Riggan et al.* [2004] report that 90% of the radiant energy emitted from burning Brazilian savannah and forest was associated with emitter temperatures in the 830–1440 K range, and therefore the temperature range over which FRP_{MIR} retrieval is optimised is quite well matched to reality. However, it is expected that combustion temperatures below 665 K may occur in smoldering-dominated fires, though *Ohlemiller* [1995] suggests this is approaching the lower temperature limit of smoldering combustion. The MIR radiance method will increasingly underestimate FRP_{TRUE} as emitter temperature decreases below 665 K, and this is the methods main potential disadvantage when compared to the bi-spectral approach, and is the reason why the latter maybe preferable when a sufficiently large and accurately quantifiable fire pixel signal is available in the TIR spectral channel. This will particularly be the case for airborne [*Riggan et al.*, 2004] and higher spatial resolution satellite imagery from sensors such as BIRD HSRS [*Zhukov et al.*, 2005a]. Analysis of data from lower spatial resolution sensors, such as MODIS and geostationary imagers may, however, benefit significantly from application of single-waveband approaches.

[18] In contrast to the MIR radiance method, which was designed as a generic approach for sensors with a MIR spectral band [*Wooster et al.*, 2003], the MODIS method was designed specifically for use with that sensor [*Kaufman et al.*, 1998a, 1998b] and is optimised for the dynamic range of the MODIS MIR 'fire' channel (band 21), which saturates at a radiative brightness temperature of $\sim$500 K, equivalent to a fire FRP of $\sim$1600 W.m^{-2} when averaged over a MODIS 1 km^2 nadir pixel. Since the vast majority of fires will be highly subpixel when observed by MODIS, this dynamic range is well-adapted for avoiding sensor saturation in the MODIS MIR 'fire' channel over all but the most intense fires. However, unlike for MODIS, in ground-based active fire remote sensing it is possible that flaming activity can entirely fill pixels, leading to brightness temperatures equal to the radiometric temperature of the hottest flames (equivalent to an FRP exceeding 200,000 W.m^{-2}). Figure 3 indicates that, while both the MODIS and MIR radiance methods provide excellent FRP retrieval capabilities within the dynamic range of MODIS' band 21, retrievals made much above a true FRP of 1600 W.m^{-2} are dramatically overestimated by the MODIS method since its coefficients were not designed to cope with such observations. The MIR radiance method is, therefore, the best single waveband retrieval approach for situations where fire fractions are

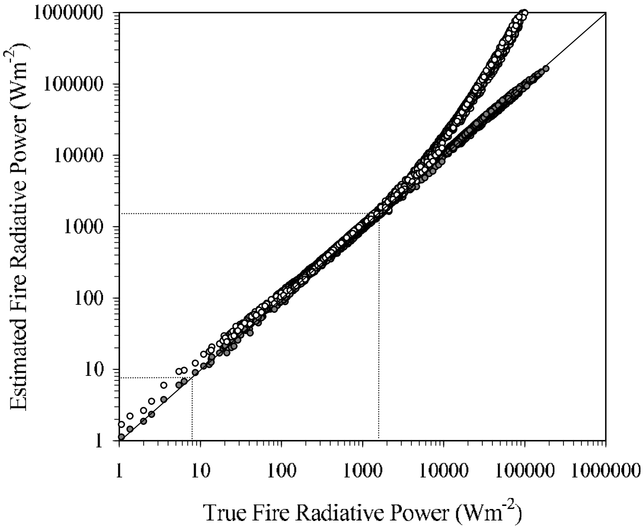

Figure 3. Comparison of the true Fire Radiative Power (FRP_{TRUE} calculated via equation (2) and expressed as a value per m^2 of the fire pixel) to that derived via the MODIS method (FRP_{MODIS} calculated via equation (3); open circles) and MIR radiance method (FRP_{MIR} calculated via equation (5); solid circles). The comparison is made for a pixel containing a two-thermal component fire whose temperatures range randomly between 600 and 1400 K and whose component proportions in a pixel range from 1.0×10^{-7} to 5.0×10^{-1}. Vertical lines approximate the minimum FRP detectable via MODIS (taken as that equivalent to a fire which raises the MIR pixel brightness temperature by ~6 K above a 300 K background) and the FRP that saturates the MODIS low-gain MIR 'fire' channel (a pixel integrated brightness temperature of 500 K in band 21).

potentially large, and the method was adopted for the ground-based experiments described here since when viewing from close distances it is possible that flames will, in fact, sometimes entirely fill a MIR pixel.

[19] FRP ($W.m^{-2}$) calculations made by equations (2), (3), or (5) can be converted into an estimate of the total FRP emitted from the subpixel fire (i.e., FRP in Watts) via multiplication by the area of the ground projection of the sensor FOV (A_{sampl}), which generally varies with viewing angle. *Wooster et al.* [2003] provide a full parameterisation of equation (5) for both MODIS and the BIRD Hotspot Recognition Sensor (HSRS), using the MIR channel central wavelength to approximate the channel's spectral response function. Adaptation for use with MIR data from other sensors is simply a matter using the channel's differing spectral sensitivity to recalculate the parameter a in the $B(\lambda, T) = aT^4$ approximation. This is most accurately performed for the expected fire temperature range (e.g., $600 < T_f < 1400$ K) via convolution of Planck's Radiation law $B(\lambda, T_f)$ and the sensor MIR spectral response function, and calculating the value of a that minimises the difference between the true spectral radiances and their aT_f^4 approximation. Table 1 indicates the value of a calculated via this method for the majority of commonly used EO sensors capable of FRP retrieval via the MIR radiance method, along with the MIR thermal camera used in the current experiment.

3.3. Sensitivity of FRP Retrieval to External Parameters

[20] When observing real fires, the accuracy of FRP retrievals made using the MIR radiance method can potentially differ from the idealised case shown in Figure 2 because the fire typically covers only a very small proportion of the pixel, because the recorded radiances are subject to atmospheric and other perturbing effects, and because of the already cited potential difference between the true ambient background signal within the fire-pixel and that of the surrounding nonfire pixels from which it is estimated. A modeling exercise was therefore conducted to estimate the sensitivity of the retrieval of MIR radiance-derived FRP to these effects.

3.3.1. Sensitivity Analysis Methodology

[21] *Giglio and Kendall* [2001] have previously conducted a highly detailed sensitivity analysis of the *Dozier* [1981] bi-spectral method, including the case where the fire is considered not to be a blackbody but rather an opaque gray body with emissivity <1.0. Adopting the same framework, we here use a similar approach to examine the sensitivity of the MIR radiance method to the assumptions made in the derivation of equation (5) and to the accuracy and precision of its parameterisation. We follow *Giglio and Kendall* [2001] whereby, for simplicity, the fire is assumed to comprise a single thermal component of temperature T_f covering proportion p_f of the pixel, with the remainder of the pixel having temperature T_b. Of course, a vital aspect of the MIR radiance method is its ability to provide meaningful retrievals even when the fire contains multiple temperature components, but for the current purpose the simplified case of a single thermal component fire suffices. The spectral radiance (L_λ) of a 'fire pixel' containing a subpixel sized actively smoldering or flaming fire observed during daytime (sunlit) conditions, i.e. when most fires occur, can be considered as the summation of the following six terms; emitted thermal radiance from the fire, solar and atmospheric dowelling irradiance reflected from the fire, emitted thermal spectral radiance from the nonfire background,

Table 1. Values of a for Use in Equation (3) for the MIR Spectral Channel of Different Imaging Sensors, Calculated Over the Emitter Temperature Range 650–1300 K via Least Squares Linear Regression Between the Modeled Within-Channel Emitted Spectral Radiance and the Fourth Power of the Emitter Temperature[a]

	a, $\times 10^{-9}$
Terra MODIS	2.96
Aqua MODIS	2.98
BIRD HSRS	3.33
GOES-8 Imager	3.07
GOES-9/10 Imager	3.06
GOES-12 Imager	3.08
Meteosat-8 SEVIRI	3.06
AGEMA 550	3.08

[a] Units are in Wm^{-2} $sr^{-1}\mu m^{-1}$ K^{-4}. Value of a will vary slightly with temperature range and method of fitting used, for example decreasing by, on average, 5.5% from the value shown here if the emitter temperature range is expanded to 600–1400 K (but with a consequential worsening of fit between the true emitted spectral radiance and the power law approximation for midrange 700–1200 K emitters).

solar and atmospheric dowelling irradiance reflected from the nonfire background, upwelling atmospheric thermal radiation, and some component of sensor noise. For the signal measured in a MIR spectral band (L_{MIR}), expressing these six components numerically using the same formulation as *Giglio and Kendall* [2001]:

$$\begin{aligned} L_{MIR} = {} & \tau_{MIR} p_f \varepsilon_{f,MIR} B\left(\lambda_{MIR}, T_f\right) + \tau_{MIR} p_f \left(1 - \varepsilon_{f,MIR}\right) \\ & \cdot \left(\tau_{d,MIR} I_{sun,MIR} \cos\phi + I_{atm,MIR}\right)/\pi \\ & + \tau_{MIR}\left(1 - p_f\right)\varepsilon_{b,MIR} B(\lambda_{MIR}, T_b) + \tau_{MIR}\left(1 - p_f\right) \\ & \cdot \left(1 - \varepsilon_{b,MIR}\right)\left(\tau_{d,MIR} I_{sun,MIR} \cos\phi + I_{atm,MIR}\right)/\pi \\ & + L_{atm,MIR} + \overline{Ln}_{MIR} \end{aligned} \tag{6}$$

The fires detectable from satellite EO are often considered to be blackbodies [*Robinson*, 1991; *Giglio and Kendall*, 2001] and if this is the case then the second term in equation (6) is zero.

[22] Similarly for a neighbouring nonfire pixel:

$$\begin{aligned} L_{b,MIR} = {} & \tau_{MIR} \varepsilon_{b,MIR} B(\lambda_{MIR}, T_b) + \tau_{MIR}\left(1 - \varepsilon_{b,MIR}\right) \\ & \cdot \left(\tau_{d,MIR} I_{sun,MIR} \cos\phi + I_{atm,MIR}\right)/\pi + L_{atm,MIR} + \overline{Ln}_{b,MIR} \end{aligned} \tag{7}$$

where τ_{MIR} is the upward atmospheric transmission in the sensors MIR spectral band, ϕ is the solar zenith angle, $\tau_{d,MIR}$ is the downward atmospheric transmission in the sensors MIR spectral band at angle ϕ, $I_{sun,MIR}$ is the extraterrestrial solar irradiance in the sensors MIR spectral band, $I_{atm,MIR}$ is the diffuse downwelling atmospheric irradiance in the MIR spectral band, $L_{atm,MIR}$ is the upwelling atmospheric spectral radiance in the MIR spectral band, $\overline{Ln}_{MIR}$ and $\overline{Ln}_{b,MIR}$ is the detector noise in the sensor MIR spectral band at the fire and background pixels respectively (the bar notation indicating a random variable), and the other symbols (T, ε, p) have their previously defined meanings, with subscript f corresponding to their value at the fire and b at the nonfire background.

[23] For the MIR radiance method (equation (5)) we require an estimate of the fire emitted spectral radiance in the MIR spectral band, $L_{f,MIR}$. This value is equivalent to Planck's Radiation law parameterised with the appropriate MIR wavelength and fire temperature, multiplied by the fires fractional area and emissivity. This is denoted by the $p_f \varepsilon_{MIR}$ $B(\lambda_{MIR}, T_f)$ term on the right hand side of equation (6), and its value can be obtained numerically by combining equations (6) and (7):

$$\begin{aligned} L_{MIR} = {} & \tau_{MIR} p_f \varepsilon_f B\left(\lambda_{MIR}, T_f\right) + L_{atm,MIR} + \left(1 - p_f\right) \\ & \cdot \left(L_{b,MIR} - L_{atm,MIR} - \overline{Ln}_{b,MIR}\right) + \tau_{MIR} p_f \left(1 - \varepsilon_f\right) \\ & \cdot \left(\tau_{d,MIR} I_{sun,MIR} \cos\phi + I_{atm,MIR}\right)/\pi + \overline{Ln}_{MIR} \end{aligned} \tag{8}$$

and re-arranging:

$$\begin{aligned} p_f \varepsilon_{MIR} B\left(\lambda_{MIR}, T_f\right) = {} & \frac{1}{\tau_{MIR}}\left(L_{MIR} - \left(1 - p_f\right) L_{b,MIR} + p_f L_{atm,MIR}\right. \\ & \left. + \left(1 - p_f\right)\overline{Ln}_{b,MIR} - \overline{Ln}_{MIR}\right) - p_f\left(1 - \varepsilon_f\right) \\ & \cdot \left(\tau_{d,MIR} I_{sun,MIR} \cos\phi + I_{atm,MIR}\right)/\pi \end{aligned} \tag{9}$$

Equation (9) represents the true value of $p_f \varepsilon_{MIR} B(\lambda_{MIR}, T_f)$ for use as $L_{f,MIR}$ in equation (5). Multiplying the output of equation (5) by the sensor pixel area then provides an estimate of the fire radiative power in Watts. However, certain of the parameters in equation (9), for example the fire fractional area, p_f, are unobtainable when using a single waveband approach, while others, for example the atmospheric downwelling radiation, are likely to be imperfectly known. However, by neglecting (relatively) unimportant terms, and by using appropriate assumptions, equation (9) can greatly simplified into a version capable of being easily parameterised for the estimation of $L_{f,MIR}$ from single waveband data. The first assumption is that the $p_f L_{atm,MIR}$ term on the right hand side of equation (9) will always be small compared to at least one of the first two terms and is therefore assumed negligible (the bi-spectral method makes the same assumption [*Giglio and Kendall*, 2001]). Next, the requirement to know the fire fractional area is removed by assuming that $(1 - p_f)L_{b,MIR} \approx L_{b,MIR}$, which is considered workable when p_f is sufficiently small, and as p_f increases the error introduced is considered minimal since in that case the spectral radiance of the fire pixel will be increasingly dominated by emittance from the (increasingly large) fire rather than from the much cooler ambient temperature background (since $B(\lambda_{MIR}, T_f) \ll B(\lambda_{MIR}, T_b)$ at MIR wavelengths). The final term in equation (9), corresponding to the solar and downwelling atmospheric radiation that are reflected from the fire, is assumed negligible for the same reason (and will actually tend to zero as the fire approaches blackbody behaviour, $\varepsilon_f = 1$). Finally, the last two noise terms are defined by the random perturbations to the fire and background pixels, $\overline{Ln}_{MIR}$ and $\overline{Ln}_{b,MIR}$ respectively and so are not included operationally during application of the MIR radiance FRP algorithm (though their potential effects can be assessed with knowledge of the signal noise, e.g., the sensor Noise Equivalent delta Temperature [NedT] value of the sensors MIR spectral band).

[24] Via the above simplifications to equation (9), the fire-emitted spectral radiance ($L_{f,MIR}$) for input into equation (5) reduces to the simple difference between the MIR spectral radiance of the active fire pixel (L_{MIR}) and that of the surrounding nonfire 'background' ($L_{b,MIR}$), where the latter is generally calculated as the mean signal of the N surrounding nonfire background pixels having, for example, the same land cover type and elevation as the fire pixel itself):

$$L_{f,MIR} = p_f \varepsilon_{f,MIR} B\left(\lambda_{MIR}, T_f\right) = \frac{1}{\tau_{MIR}}\left(L_{MIR} - L_{b,MIR}\right) \tag{10}$$

The simplifications used to derive equations (5) and (10) were assessed for their impact on FRP retrieval accuracy using a modeling exercise similar to that of *Gigio and Kendall* [2001]. Nominal values for all background surface and atmospheric parameters were used within equation (6) to model the actual top-of-atmosphere fire pixel radiance (L_{MIR}) that would be observed given fires of various subpixel areas, temperatures and emissivities. Similarly, equation (7) was used to model the matching top-of-atmosphere background pixel radiance, $L_{b,MIR}$. The simulation was performed assuming the MODIS sensor viewing through the 1976 US standard atmosphere, with overhead solar illumination, and a background temperature and emissivity of 300 K and 0.96 respectively. In this way the surface and atmospheric parameters listed in Table 2 of

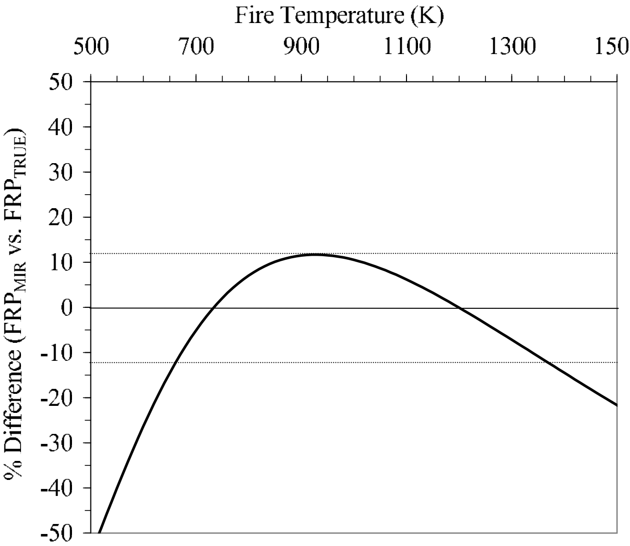

Figure 4. Percentage difference between FRP_{MIR} [calculated with equations (5) and (10) parameterised with L_{MIR} and $L_{MIR,b}$ from equations (6) and (7) using unperturbed (true) values of all parameters] and FRP_{TRUE} calculated with equation (2). Results from subpixel sized fires having fractional areas 0.0001 to 0.1 lie on the same curve (i.e., superimpose directly upon one another). Horizontal lines in denote ± 12% accuracy limits of the MIR radiance method, and the figure is seen to be essentially identical to that of Figure 2b.

Giglio and Kendall [2001] could be used for the parameterisation, and the results compared to those for the *Dozier* [1981] method if desired. For this illustration, the value of *a* used in equation (5) was that which gives the best fit for the band 21 spectral response function of the MODIS Aqua sensor over the 650–1300 K temperature range (Table 1).

[25] For each fire situation considered, an assessment of the difference between the true fire radiative power (FRP_{TRUE}, calculated from equation (2)) and the MIR radiance-derived estimate (FRP_{MIR}, derived via parameterisation of equations (5) and (10) with the modeled top-of-atmosphere values of L_{MIR} and $L_{b,MIR}$) was made. Two cases were considered. In Case 1, τ_{MIR} and $L_{b,MIR}$ in equation (10) were considered to be known perfectly and thus differences between FRP_{MIR} and FRP_{TRUE} were due only to the simplifying assumptions made during derivation of equation (10), and to the use of the power law approximation to Planck's Radiation law during the derivation of equation (5) (which itself has already been considered in Figure 2b). In Case 2, realistic perturbations were made to the assumed values of τ_{MIR}, $L_{b,MIR}$ and L_{MIR} used in equation (10) in order to represent the more likely situation where, respectively, the atmospheric transmission is imprecisely known, the neighbouring nonfire background pixels do not perfectly represent the signal from the nonfire part of the fire pixel itself (i.e., they have a different temperature and/or MIR reflectance), or the measured radiance of the fire pixel itself is perturbed by sensor noise or some other external effect. The effect of these perturbations on the retrieval of FRP_{MIR} was again assessed via its comparison to FRP_{TRUE}. Both Case 1 and Case 2 were considered for situations where the fire exhibited blackbody behaviour ($\varepsilon_f = 1$), and gray body behaviour ($\varepsilon_f < 1$).

3.3.2. Sensitivity Analysis Results

[26] Figure 4 indicates the results from the Case 1 simulations, where all parameters are known with zero error and the fire is considered a blackbody. The figure is essentially identical to Figure 2b, confirming that when the fire conforms to blackbody behaviour the assumptions made during the derivation of fire emitted MIR spectral radiance signal (equation (10)) from equations (6) and (7) introduces negligible error. Retrieval of FRP_{MIR} is actually independent of emissivity since the $\varepsilon_{f,MIR}$ and ε_f terms in equation (5) cancel. In fact, provided the fire behaves like a gray body (which is a broadly realistic assumption [*Langaas*, 1995]), even if the fire emissivity falls considerably to 0.5 for example, which represents a fire whose path length of ~1 m [*Langaas*, 1995; *Giglio et al.*, 2003] and which is thus most certainly at the lower end of fire sizes likely to be detectable from moderate resolution spaceborne data, the effect on the retrieval of FPR_{MIR} is insignificant under the Case 1 conditions. Thus the further necessary assumption made during derivation of equation (10), that the solar and downwelling atmospheric radiation reflected by the fire under such nonblackbody conditions is negligible when compared to the other terms, is also seen to be correct.

[27] Results from the first situations considered in Case 2 are shown in Figure 5, where the background radiance $L_{b,MIR}$ was perturbed prior to input into equation (10). For any particular fire temperature, at zero perturbation ($\Delta L_{b,MIR} = 0$) the results are identical for all fire fractional areas. It is for this reason that the lines representing results for each fire size converge at the $\Delta L_{b,MIR} = 0$ point, and also why the same lines superimpose upon on one another in Figure 4. As $\Delta L_{b,MIR}$ increases away from zero, FRP_{MIR} is generally only very weakly affected for the range of $\Delta L_{b,MIR}$ perturbations previously considered by *Giglio and Kendall* [2001] (-0.02 to $+ 0.02$ Wm^{-2} sr^{-1} μm^{-1}; equivalent to ±0.75 K at 300 K). Perturbations of this level change the absolute level of agreement between FRP_{MIR} and FRP_{TRUE} of detectable fires by a maximum of 8% (for a 600 K fire of fractional area 0.001). Only in situations where the fires are, in any case, very unlikely to be detectable do $\Delta L_{b,MIR}$, perturbations of this size have a significant influence on FRP_{MIR} (i.e., 600 K fires of fractional area 0.0005 or smaller, and 800 K fires of fractional area 0.0001 or smaller). For completeness, we also consider the effect of much larger $\Delta L_{b,MIR}$ perturbations (-0.4 to $+ 0.4$ Wm^{-2} sr^{-1} μm^{-1}; equivalent to -21 to $+ 12$ K at 300 K) which may feasibly result when, for example, the fire or background pixels contain large, recently burned areas. Such areas of ash and char may still be cooling, and in any case in direct sunlight their low albedo can increase their temperature markedly above that of neighbouring unburned (live) vegetation. If one third of neighbouring background pixel is covered by a recently burnt area having a temperature 33 K above ambient, then the pixel MIR brightness temperature would be increased by 12 K. Figure 5 indicates that for the smallest detectable 600 K fire (fractional area 0.001) the error on FRP_{MIR} introduced by a $\Delta L_{b,MIR}$ perturbation of -0.4 to $+ 0.4$ Wm^{-2} sr^{-1} μm^{-1} ranges from +90% to

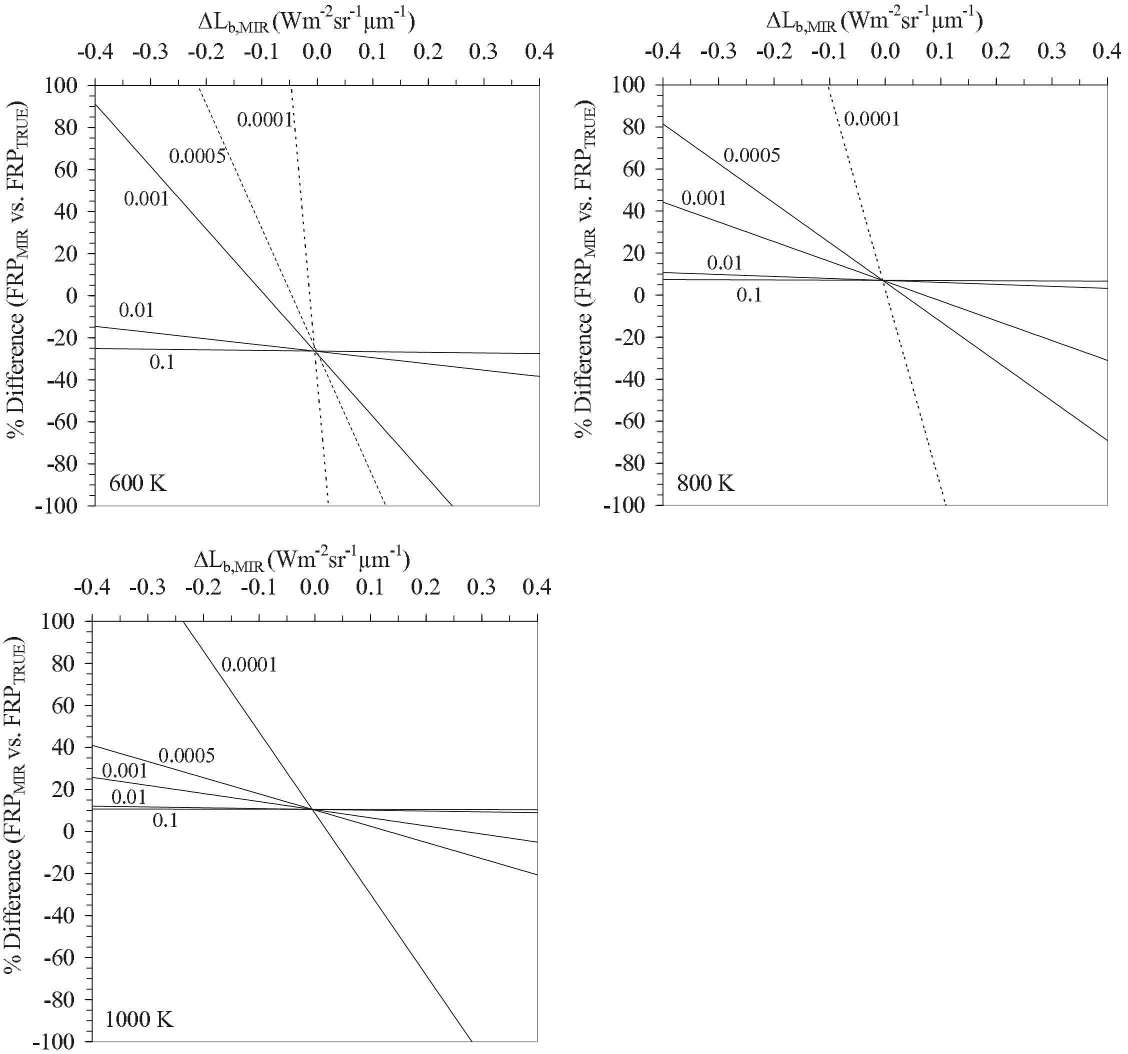

Figure 5. Departure of FRP_{MIR} from FRP_{TRUE} for blackbody fires of temperature 600, 800 and 1000 K and fractional areas 0.1 to 0.0001 (denoted by the labels) as a function of the level of disagreement ($\Delta L_{b,MIR}$) between the assumed background radiance signal ($L_{b,MIR}$ in equation (10)) and its true value. Dotted lines indicate situations where the fire may be too cool and/or small to be robustly detectable (i.e., the MIR brightness temperature is raised by less than 6 K over that of surrounding nonfire pixels). At $\Delta L_{b,MIR} = 0$ results for each fire temperature converge, indicating the insensitivity of the error to fire fractional area under this condition.

−140%. For 800 K and 1000 K fires of the same size, the error magnitude is reduced by up to a factor of seven, and fires of fractional area 0.01 or greater show minimal sensitivity to even this large range of $\Delta L_{b,MIR}$. These results indicate the value of choosing nonfire pixels that are best-matched to the land cover type of the fire pixel itself when characterising $L_{b,MIR}$ in satellite EO data. As such, when analysing multi-spectral spaceborne imagery, it maybe useful to consider the spectral reflectance profiles of the fire and background pixels to allow their degree of similarity (e.g., in subpixel burned area) to be at least approximately assessed (though smoke may hinder this comparison at shorter wavelengths). However, it should also be considered that the range of variation seen in the MIR spectral radiance of the background pixel set surrounding a fire pixel is quite typically an order of magnitude smaller than the ±0.4 $\mathrm{Wm^{-2}\ sr^{-1}\ \mu m^{-1}}$ maximum range considered here, and while this does not directly tell us the actual difference between the signal of these pixels and that of the ambient background signal of the fire pixel itself (i.e., $\Delta L_{b,MIR}$), this small level of variation suggests that $\Delta L_{b,MIR}$ could also be of a magnitude where any resultant error on FRP_{MIR} is minor.

[28] Figure 6 indicates the sensitivity of the FRP retrievals to the estimate of MIR atmospheric transmission (τ_{MIR} in equation (10)), and how this interacts with sensitivity to the uncertainties in $L_{b,MIR}$ assessed previously in Figure 5. Transmission in the MIR atmospheric window is controlled in part by the atmospheric water vapour concentration, which is spatially and temporally variable. Therefore τ_{MIR} is unlikely to be known precisely. However, transmission in the MIR spectral region is considerably less sensitive to such water vapour variations than is transmission in the longer wavelength TIR region, and so it seems

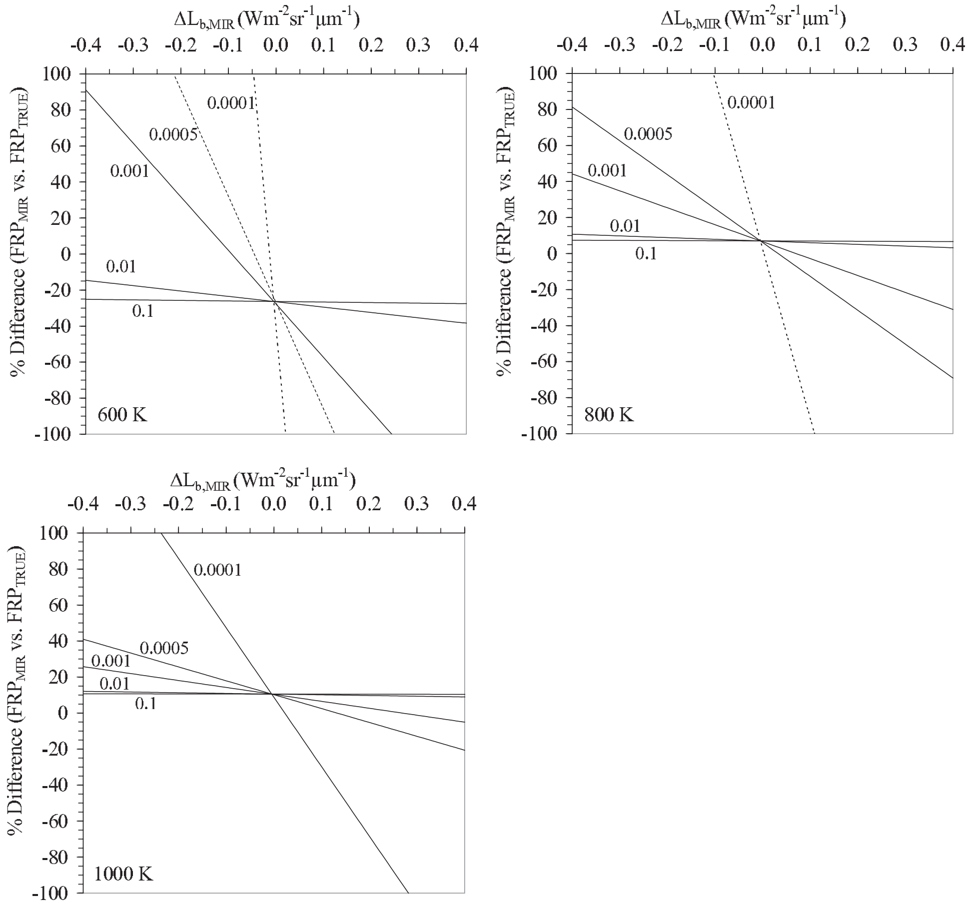

Figure 6. Departure of FRP_{MIR} from FRP_{TRUE} for an 800 K blackbody fire of fractional area 0.1 to 0.0001 (denoted by the labels) as a function of the level of disagreement ($\Delta L_{b,MIR}$) between the assumed background radiance signal ($L_{b,MIR}$ in equation (10)) and its true value. A 15% underestimate in the assumed MIR atmospheric transmission (τ_{MIR} in equation (10)) may be assumed in Figure 6a, perfect knowledge in Figure 6b, and a 15% overestimate in Figure 6c. Dotted lines indicate situations where the fire is too cool and/or too small to be robustly detectable (i.e., the MIR brightness temperature is raised by less than 6 K over that of surrounding nonfire pixels). At $\Delta L_{b,MIR} = 0$ results for each fire temperature converge, indicating the insensitivity of the error to fire fractional area under this condition.

probable that τ_{MIR} can be estimated to, for example, ±15% precision. Using an 800 K fire as an example, the effect of an error of ±15% in the assumed value of τ_{MIR} was assessed (an overestimate of 15% being, in fact, equivalent to no atmospheric correction being performed; i.e., an assumed τ_{MIR} of unity). For such a fire, Figure 6b confirms that perfect knowledge of both τ_{MIR} and $L_{b,MIR}$ allows the maximum error in FRP_{MIR} to remain lower than +10% when compared to FRP_{TRUE} for all fire fractional areas. As would be expected via examination of equation (10), if $L_{b,MIR}$ continues to be known perfectly (i.e., $\Delta L_{b,MIR} = 0$) then a 15% underestimate in τ_{MIR} increases the magnitude of the FRP overestimate derived via the MIR radiance method, to ~25% for all detectable fires (Figure 6a). Conversely, a 15% overestimate in τ_{MIR} turns the previously overestimated FRP into an underestimate of ~10% (Figure 6c), again assuming $\Delta L_{b,MIR} = 0$. For nonzero values of $\Delta L_{b,MIR}$, the interaction of errors in assumed τ_{MIR} and $L_{b,MIR}$ causes these effects to be magnified (see Figures 6a, 6b, and 6c for $\Delta L_{b,MIR} = \pm 0.4\ Wm^{-2}\ sr^{-1}\ \mu m^{-1}$; though it should be recalled that such large values of $\Delta L_{b,MIR}$ in fact represent a rather large (−21 to +12 K) error in characterisation of the fire pixel background signal; assuming the ambient temperature is ~300 K).

[29] The Case 2 situation where the observed top-of-atmosphere fire pixel radiance (L_{MIR}) is over or underestimated is, in fact, numerically equivalent to, respectively, an under- or overestimate of $\Delta L_{b,MIR}$, since equation (10) shows that the retrieval of MIR_{FRP} is simply driven by the difference between these two measures. Therefore, Figure 5 can also be used to ascertain the effect of perturbations to the measured L_{MIR} away from its true value. Such perturbations may include sensor noise, which for low gain systems such as MODIS band 21 can reportedly reach ~0.06 Wm^{-2} sr^{-1} μm^{-1} (equivalent to a 2 K NEdT at 300 K), but which for standard gain sensors are typically an order of magnitude lower. Furthermore, being random, such noise levels are reduced by averaging when analysing the set of background pixel signals to obtain $L_{b,MIR}$, and in the case of MODIS the $L_{b,MIR}$ values are in any case typically obtained

Table 2. Characteristics of the GER3700 Spectroradiometer and AGEMA 550 MIR Thermal Camera

Instrument	GER 3700 Spectroradiometer	AGEMA 550 Camera
Type	704 spectral channels, nonimaging sensor	1 spectral channel, imaging sensor
Nominal spectral range	0.4–2.5 μm	3.6–5.0 μm
Detector type	3 dispersion gratings VNIR 350–1050 nm: Si array SWIR1 1050–1900 nm: PbS SWIR2 1900–2500 nm: PbS	PtSi focal plane array (320 × 240 pixels)
Field-of-view	10° circular Most sensitive over 70% of this area [*Schaepman*, 1998]	20° × 15° rectangular
Detector thermal stability	Varies with ambient conditions	Cooled to 77 K
Spectral-resolution	3–16 nm (varies with wavelength)	3.9 μm narrowband filter
Measurement interval	5 seconds	1 second

not from the low-gain band 21 data but rather the data from the standard-gain channel having the same wavelength range (band 22). Figures 5 and 6 indicate that such levels of over- or underestimation of L_{MIR} have little significant effect on the retrieved MIR_{FRP}, simply because these perturbations are small in comparison to the absolute value of L_{MIR} for the sorts of fire pixels that are robustly detectable.

[30] This sensitivity analysis indicates that in cases where the MIR radiance method is applied to data where the fire components are expected to dominate the pixel FOV, and the pixel area and atmospheric transmission is accurately known, then retrieved FRP is totally insensitive to parameterisation error. Such conditions conform well to those found in the field experiment described in section 4, and in this case the only significant uncertainty introduced by the method is that inherent in the power law approximation to Planck's Radiation law (Figure 4). When the method is applied to spaceborne data, where there is a quantifiable uncertainty in the assumed MIR background signal of the fire pixel (assessed via the variation in the surrounding background nonfire pixel signals) and in the atmospheric transmission, the expected range of these parameters can be used to place error bars on the determination of FRP.

4. Field Experiment Methodology

4.1. Remote Sensing Data and Calibration

[31] During the field experiment, remote sensing of fire-radiated energy was conducted using two complementary instruments (Table 2). A GER 3700 field spectroradiometer provided measurement of the fires spectral emittance at multiple wavelengths in the 0.4–2.5 μm spectral region, while a MIR camera fitted with a 3.9 μm narrowband filter provided pixel brightness temperature imagery in the same spectral interval covered by the MODIS MIR 'fire' channel. The MIR camera was continually self-calibrated and was cooled to 77 K via means of an onboard blackbody and Stirling-cycle cooler, providing an absolute accuracy of ±2% within the brightness temperature range 480–1023 K.

[32] The GER3700 spectroradiometer records data as raw digital numbers, which are converted to incoming spectral radiance measures via a set of calibration constants provided by the NERC Equipment Pool for Field Spectroscopy (EPFS), from where the instrument was loaned. In the case of fires, great care must be taken when performing this calibration since the instrument is primarily designed to observe static rather than dynamic phenomena. In particular, the 'spectral matching' feature of the instruments measurement procedure, whose nominal aim is to correct for any discontinuity in the measured spectrum that may appear at the 1050 nm junction of the detector arrays covering the 350–1050 nm (VNIR) and 1050–1900 nm (SWIR1) spectral regions, can induce unwanted effects. This spectral matching process adjusts data from both SWIR1 and SWIR2 arrays (measured by PbS detectors; Table 2) by a factor derived from matching data in the 1050 nm VNIR-SWIR1 overlap region, the assumption being that the radiant sensitivity of the VNIR Si photodiode array is temperature independent, unlike that of the PbS detectors whose response can vary with ambient temperature and thus produce a measurement discontinuity. This procedure is ill-suited to observing rapidly-varying phenomena such as fires however, since the VNIR, SWIR1 and SWIR2 spectroradiometric signals are collected at slightly different times (max. 50 ms difference) and the fire may not meet the inherent supposition of a temporally consistent radiation source over this period. Furthermore, during daytime observations the VNIR signal is dominated by solar-reflected radiation and the SWIR1 and SWIR2 by fire-emitted radiation. The relevance of this spectral matching procedure to temporally dynamic phenomena was not fully appreciated at the time of the *Wooster* [2002] study, and so its impact is present in those results. For the current experiment the GER3700 data collection routine was customised to allow data collection and calibration without spectral matching, with the PbS detector temperature monitored and a manual adjustment made for its temperature dependent response. The radiometric accuracy of this approach was confirmed using multiple observations of a laboratory blackbody at various instrument and calibration source temperatures; the results indicating absolute radiometric accuracies within 10% at most wavelengths longer than ~1.5 μm (Figure 7).

4.2. Fuel Types

[33] Dead fuels were used in order to replicate conditions found during most dry season savanna fires, which were the ultimate target for our spaceborne FRP investigations [*Roberts et al.*, 2005]. The primary fuel was *Miscanthus*, a tall perennial grass chosen because its large leaf mass minimised the disruption of the fuel bed by wind, and because its burning characteristics are well known due to its use in biomass energy applications [*Scurlock*, 1999]. The *Miscanthus* leaves were dried to a gravimetric moisture content of 12% (determined by oven drying) and chopped

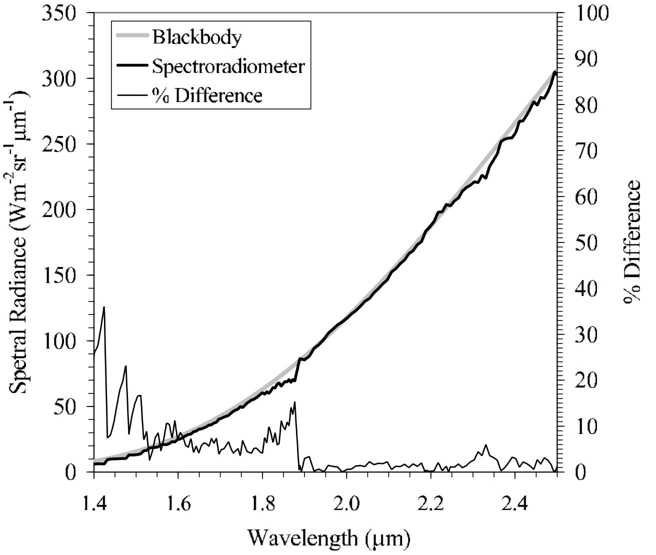

Figure 7. Comparison of the spectral radiance emitted by a 695 K blackbody and that measured by the GER 3700 field spectroradiometer in the spectral range 1.4–2.5 μm using the spectro-radiometric calibration method developed for this study.

into 2–10 cm long sections. Other herbaceous fuels used were dried grasses and wheat stems, along with a woody component of dried chips of oak and hickory. Dead fuel moisture content (FMC) is governed by ambient environmental conditions, specifically temperature, humidity, and wind speed [*Rothermel et al.*, 1986]. The time required for fuel moisture to reach equilibrium with the ambient environment is largely a function of the fuel particle diameter; hence the partitioning of fuel into Equilibrium Moisture Content (EMC) time lag classes [*Rothermel et al.*, 1986]. Our herbaceous fuels represented a one-hour EMC class, the oak a 10-hour class, and the hickory a >100-hour class. All fuels were stored outside but under cover, such that they were able to equilibriate to the ambient conditions, and over the May to August 2003 period of the experiment this provided varying FMC values such as are found in natural fires since air temperatures ranged from 17–38°C and relative humidity from 30–60%.

4.3. Experimental Design and Measurement Procedure

[34] Figure 8 illustrates the experimental setup, around which a 1.5 m high partition was placed to minimise the effect of wind on the fuel, and in particular on the measurements of fuel mass and combustion rate. The fuel bed was constructed atop a 1.5 × 1.2 m tray, filled with sand to a depth of 4 cm and mounted on digitally-logged scales with 0.005 kg precision. Fuel was arranged in a variety of spatial distributions, from a ~1 cm deep horizontally uniform layer covering the tray, to individual fuel piles up to 0.15 m deep. The remote sensing instruments were mounted 11.5 m above the fuel bed, viewing directly downwards and carefully aligned so that their fields of view were centred on the middle of the fuel bed, providing a 2 m diameter circular FOV for the spectroradiometer and a 4 × 3 m field of view (pixel size 1.27 × 1.27 cm) for the MIR camera. Between three and eight fires were conducted per day, and horizontal and vertical video records and logs of the meteorological conditions were obtained for each.

[35] Fires were ignited via application of a flame to the upwind edge of the fuel bed, and the MIR camera, digital scales and spectroradiometer data logged at 1 Hz, 1 Hz and 0.2 Hz, respectively over the fire duration. Initial tests indicated that the sensitivity of the spectroradiometer to targets within its nominal field of view decreased dramatically outside of a central 1 m diameter circle. Therefore only fires where the fuel bed was confined to the centre 0.8 × 0.8 m of the tray were used for spectro-radiometeric analysis. The MIR camera showed no such spatial sensitivity, and data from all fires were analysed using this instrument. A total of forty-six fires were conducted where useable data were collected throughout, with initial fuel mass varying from 0.07–6.00 kg.

4.4. Data Processing

[36] For each analysed fire, contemporaneous fire radiative power data were derived via a spectro-radiometric approach based on the emission spectra recorded by the GER3700, and via the MIR radiance method applied to the MIR camera imagery.

4.4.1. Spectroradiometer-Derived FRP

[37] Example fire emission spectra are shown in Figure 9a. FRP were derived from each spectrum using the approach described in detail in *Wooster* [2002], based on that originally developed by *Flynn et al.* [1993] for the radiometric analysis of active lava flows. As shown by Planck's Radiation law, the shape of any spectral radiance emittance curve over the wavelength range measured by the spectroradiometer is unique to a particular emitter temperature. The spectroradiometric FRP retrieval approach exploits this feature to derive the characteristics of the two 'effective emitters' in equation (11) whose summed spectra (S_{mod}) most closely match those of the measured spectra in the wavelength region where the solar reflected radiation contribution is small compared to the radiant emission contribution from the fire, where the spectroradiometer is well calibrated (Figure 7), and where the atmosphere has minimal effect on the measured spectra (i.e., at selected wavelengths longer than 1.5 μm):

$$S_{\mathrm{mod}}(\lambda) = \sum_{k=1}^{2} p_k L_k(\lambda, T_k) \qquad (11)$$

where $L(\lambda, T)$ is the spectral radiance calculated by Planck' Radiation law, T_k is the effective emitter radiometric temperature (K), and p_k is the effective emitter fractional area. Since fires did not fill the instrument FOV, there is no requirement for the fractional areas of the individual components to sum to unity, and the instrument design means that inter-channel spatial misregistration and point spread function effects can be neglected.

[38] Once the effective emitter temperature and size characteristics are obtained from equation (11), they are used with the Stefan-Boltzmann law to calculate the total FRP emitted over all wavelengths (Figures 9b and 9c). FRE is then calculated via temporal integration of FRP recorded over the fire duration.

4.4.2. MIR Camera Derived FRP

[39] The MIR camera was sensitive to radiance signals equivalent to MIR pixel integrated brightness temperatures

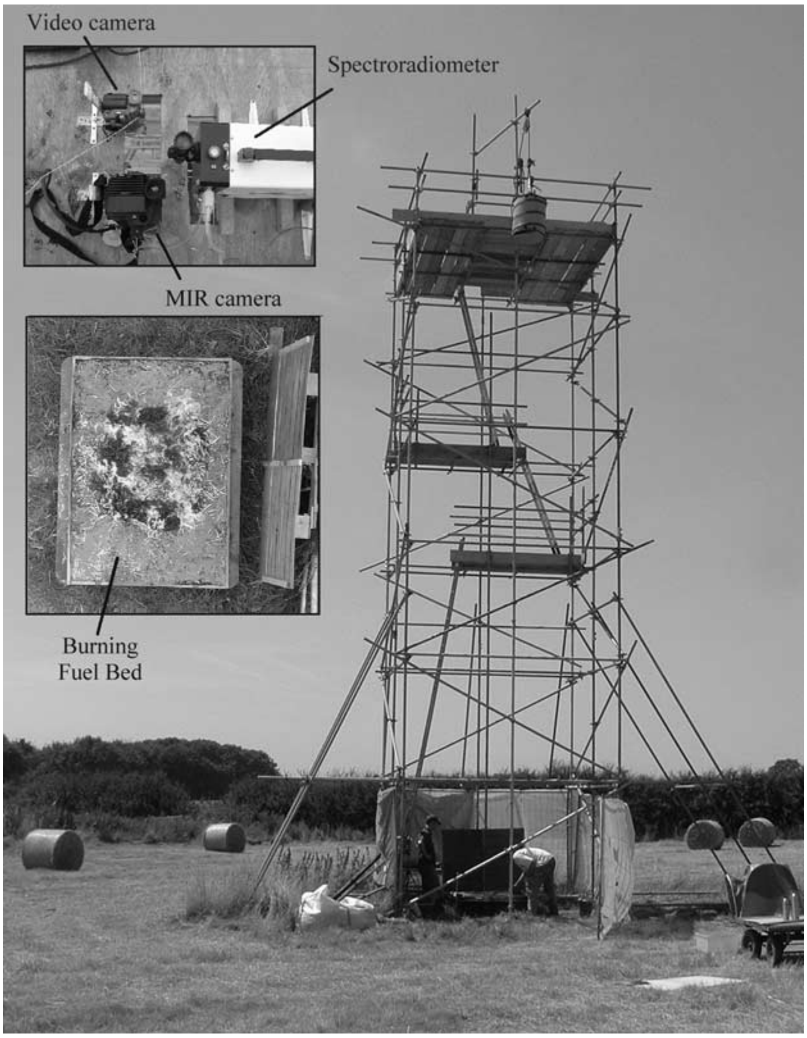

Figure 8. Experimental geometry, where a 11.5 m high scaffold tower (main picture) allowed the remote sensing instruments (upper inset) to view vertically downward onto the fuel bed (lower inset).

exceeding 475 K. Tests indicated that a 477 K threshold effectively separated the active fire pixels within each image, which typically numbered in the many thousands at the combustion rate peak. To these pixels, the MIR radiance FRP retrieval algorithm was applied (equations (5) and (10); with *a* determined for a 650–1300 K emitter temperature range as it was for the simulations shown in Figures 2–6) and the results summed to obtain a 'per fire' FRP. Again, FRE was calculated via temporal integration of FRP over the fire duration. It is important to realise that the radiometric temperatures of the recorded fire pixels do not necessarily represent the temperature of the fire itself, since the fire component within each pixel could of course be subpixel sized even at this highly detailed spatial scale.

[40] Figure 10 shows an example FRP time-series, derived via this approach for a single fire. FRP increases to a peak, corresponding to when the flaming front encompasses the entire fuel bed, and then decreases. This decrease continues as flaming begins to cease in parts of the fuel bed, either because the fuel is fully burnt, or where the surface layer of ash and char inhibits the oxygen supply required for flaming combustion of the underlying layers (in this case smoldering combustion may commence and proceed for some considerable time). Ultimately all combustion stops, the fuel bed cools, and radiative energy emission above the ambient background falls ultimately to zero.

[41] Figure 10 in fact includes two FRP time-series retrievals derived from the same imagery, calculated using both the MIR radiance method and the simple application of the Stefan-Boltzmann law to the fire pixel radiometric temperatures. The extent to which the two approaches agree depends on the pixels thermal homogeneity (which the Stefan-Boltzmann method assumes but the MIR radiance method does not) and the nature of the fires radiometric temperature distribution (since, as Figures 2 and 4 show, the MIR radiance method can over- or under-estimate the FRP from individual subpixel fire components depending on their temperature). In this example, the two retrieval methods provide virtually identical results up to, and immediately beyond, the FRP peak, after which the MIR radiance method starts to provide lower estimates. This pattern was the same for all fires, and results from the fact that the fire component forms a large fraction of the pixel area (so the Stefan-Boltzmann method performs well), and after the FRP

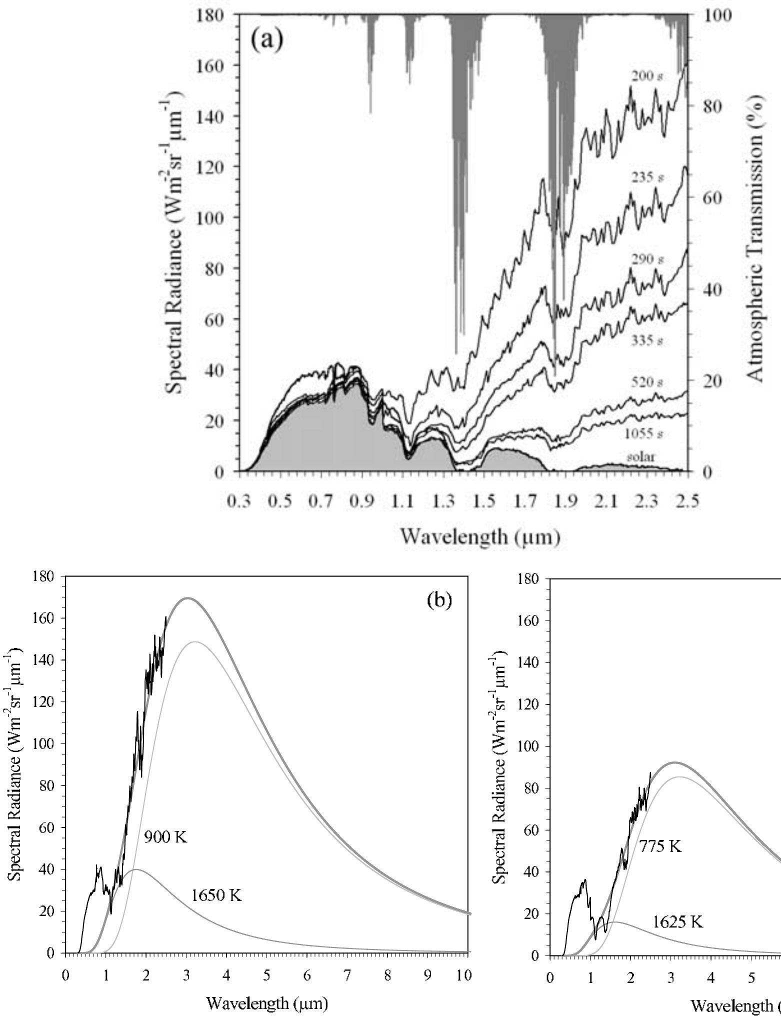

Figure 9. Spectro-radiometric data and model fits for an active fire burning 3 kg of herbaceous fuel. (a) Example spectra collected between 200 and 1055 seconds after fire ignition, along with the atmospheric path transmissivity modeled using MODTRAN 3.7 [*Anderson et al.*, 1995]. Dips in the recorded spectra are seen to match spectral regions where atmospheric transmission is low. Note how the shape and magnitude of the radiative emittance curve varies with time, becoming more and then less intense as the fire intensifies and subsides. At wavelengths shorter than ~1.5 μm the raw spectra are dominated by solar reflected radiation, whose spectral distribution prior to the fire is also shown. (b) and (c) Examples of fire radiative power retrieval from two such spectra taken at 200 and 290 seconds, respectively. The measured spectra and the most closely fitting two-component model are shown in each case, with model fitting based on spectral measurements longer than 1.5 μm outside of the atmospheric absorption bands. The modeled spectra, derived from the summed radiative emission of two 'effective emitters' that are also shown, can be extended to any wavelength (here to 10 μm) and is used to derive the instantaneous fire radiative power from each spectra. In the cases shown the effective emitters have temperatures of 1650 K and 900 K, with the cooler emitter being 77× larger (Figure 9b), and 1625 K and 775 K, with the cooler emitted being 190× larger (Figure 9c).

peak progressively larger areas of the fuel bed cool to below ~750 K, below which temperature FRP begins to be somewhat underestimated by the MIR radiance method (Figures 2b and 4). Despite this, because the two contrasting FRP retrievals only diverge by marginal amounts for the majority of the fires lifetime, and agree very well during the most intense periods of radiant energy emission, the FRE calculated from temporal integration of each FRP time-series differs by only 12.2%. The same comparison was made for other fires, producing a mean difference of 14.0 ± 1.1% (mean ± 1 SD).

5. Results

5.1. FRP Comparison via Alternative Approaches

[42] Figure 11 compares results derived via the spectro-radiometric and MIR-radiance approaches. In terms of FRE, the estimate derived via the spectro-radiometric approach is

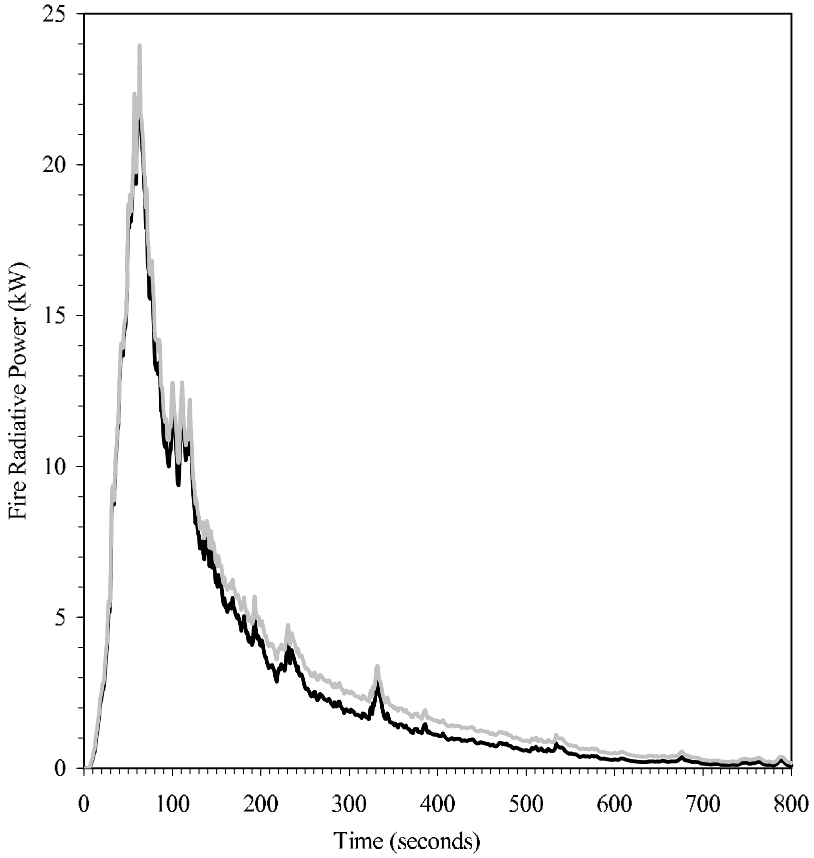

Figure 10. Fire radiative power time-series derived from MIR camera imagery of a 1.25 kg fire of herbaceous fuel conducted on 4 August 2003, via the MIR radiance method (equation (5), black line) and the Stefan-Boltzmann law (equation (2), grey line).

generally higher; which is likely to result from a combination of the following factors:

[43] 1. The MIR camera only includes FRP from pixels with a radiometric brightness temperature of 477 K or higher. Clearly all of the flaming and smoldering areas will be hotter than this, but if their proportion in any particular pixel is sufficiently small then the pixel's overall radiometric brightness temperature can lie below this threshold. Furthermore, areas where the fire has extinguished will cool below this threshold and so will not be included in the MIR radiance-derived FRP, though such areas can contribute to the spectro-radiometric FRP.

[44] 2. The MIR-radiance method begins to underestimate FRP for fire temperatures >1200 K (Figures 2b and 4), and during flaming phases emitter temperatures hotter than this will be present at the subpixel scale. Underestimation also occurs for fire temperatures <725 K, which will become increasingly dominant as a fire progresses through the latter stages of the smoldering phase.

[45] 3. The fire was located at the centre of the GER3700 field of view, and it is possible that the instrument maybe somewhat more sensitive to features within the central part of the FOV than to features located more toward the FOV edge.

[46] Given the instrument differences and the limitations of each FRP retrieval approach, the comparison shows that the spectro-radiometric and MIR radiance methods of FRP and FRE retrieval agree well, and this provides confidence in the ability of the MIR radiance method to derive FRP using a single waveband approach. Since only the MIR radiance method is applicable to existing satellite EO imagery, and in particular the lower spatial resolution imagery that can provide high temporal resolution FRP retrievals from which FRE can feasibly be calculated, all further estimates of FRP and FRE considered here use this approach.

5.2. Emitted Energy and Fuel Consumption Relationships

5.2.1. Fire Radiative Power and Combustion Rate

[47] Fuel mass (loss) data were sometimes affected by wind, by convection currents induced by the fire, and possibly by the heat causing expansion and contraction of the weighing apparatus. Nonlinear best fits to the raw mass data were used to minimise this noise (e.g., Figure 12a), and combustion rate calculated as the derivate of the fuel mass function with respect to time. The combustion rate was compared to the simultaneously recorded FRP time series (Figure 12b), and was found to show a relationship well-fitted by a linear approximation (Figures 12c and 12d). However, examination of Figure 12b indicates that while the combustion rate falls to zero after nine minutes, FRP remains elevated for a further three minutes. This is due to the ash, char and sand of the fuel bed having absorbed heat during the combustion process, a percentage of which is then re-radiated toward the end of the fire. In this case 9%

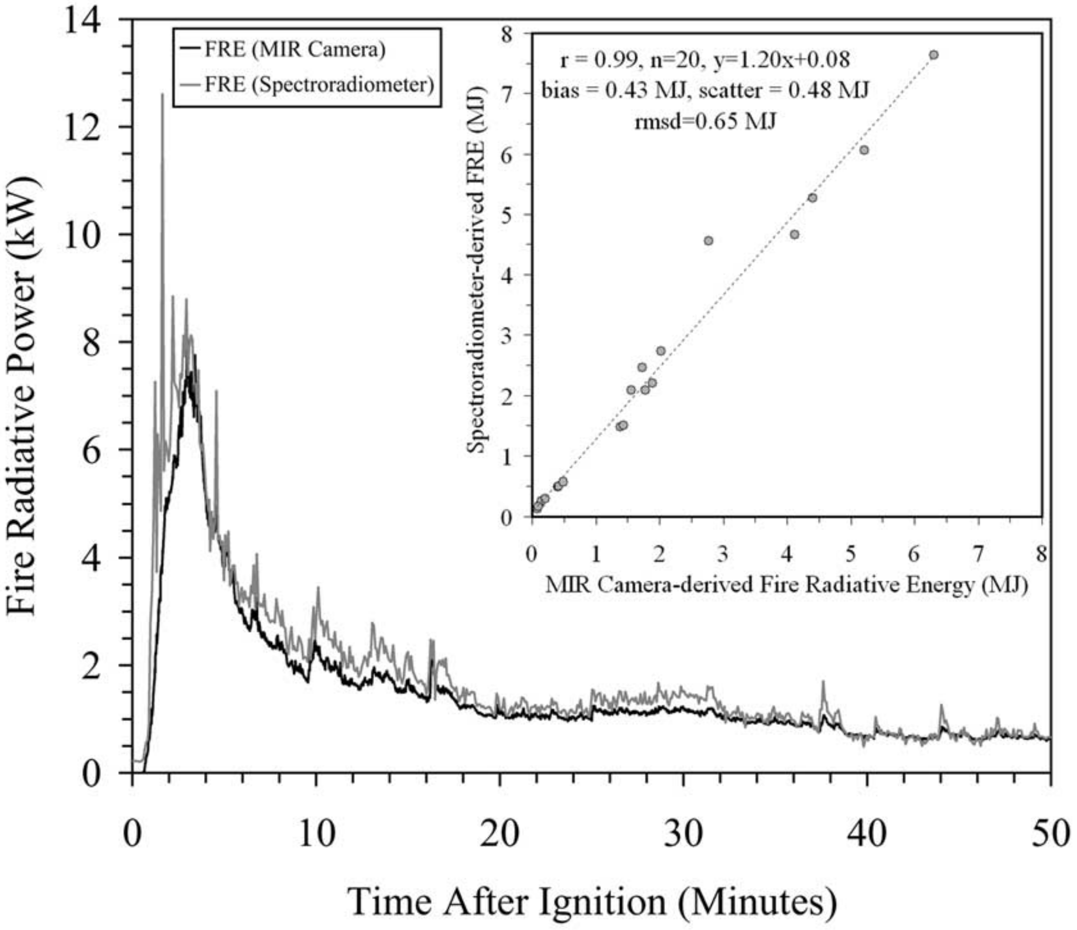

Figure 11. Comparison of fire radiative power and fire radiative energy derivations made via the spectro-radiometric and MIR radiance methods. Main plot shows the FRP time series derived via the spectro-radiometric (grey line) and MIR radiance (black line) methods for the 3 kg fire whose spectra were shown in Figure 9. The strong agreement between the two methods is evident, with most significant differences at times of increased flaming, represented by local FRP peaks. Fire radiative energy (i.e., time-integrated FRP) is 15% higher for the spectro-radiometric method in this case. The inset shows comparison of spectro-radiometric and MIR camera derived FRE for all fires whose characteristics allowed the application of both techniques (recalling that only the smaller area fires were suitable for spectro-radiometric analysis), with the ordinary least squares (OLS) linear best-fit indicated. Again the higher FRE derived via the spectro-radiometric method is evident.

of the total FRE recorded is emitted after the seven-minute stage, where the FRP and combustion rate curves start to diverge, and 1% of total FRE is emitted after the nine-minute stage, when combustion has ceased completely. Figure 13 shows data extracted from all *Miscanthus* fires, where a linear relationship between combustion rate and FRP can again be seen:

$$\text{Combustion Rate}\left(\text{kg.sec}^{-1}\right) = 0.464(\pm 0.018) \times 10^{-3}.\text{FRP}(\text{ kW}) \qquad (12)$$

The parameter 0.464 kg.MJ^{-1} is the radiant energy ‘combustion factor’, relating the rates of radiative energy release and fuel consumption. The relationship is forced through the origin, assuming zero FRP indicates no active combustion. Examining the data of each fire separately (not shown), it is apparent that for a minority of fires the combustion rate corresponding to a particular FRP is significantly greater before the fire reaches its maximum combustion rate than it is after this point. The effect can be seen to some extent in Figure 12b (compare data recorded at 0–2 minutes versus that at 7–12 minutes) and is responsible for the slight hysteresis seen in the data of Figure 10c. This effect results from the fact that once combustion has reached its maximum rate, areas of the fuel bed that are subsequently extinguished continue to contribute FRP as they lose stored heat via re-radiation while cooling to ambient.

5.2.2. Fire Radiative Energy and Total Mass Consumed

[48] For all fires, FRE shows an excellent linear relationship with total fuel mass consumed (Figure 14), with the latter calculated as the difference between pre- and post-fire mass. Converting each datapoint to the ratio between FRE

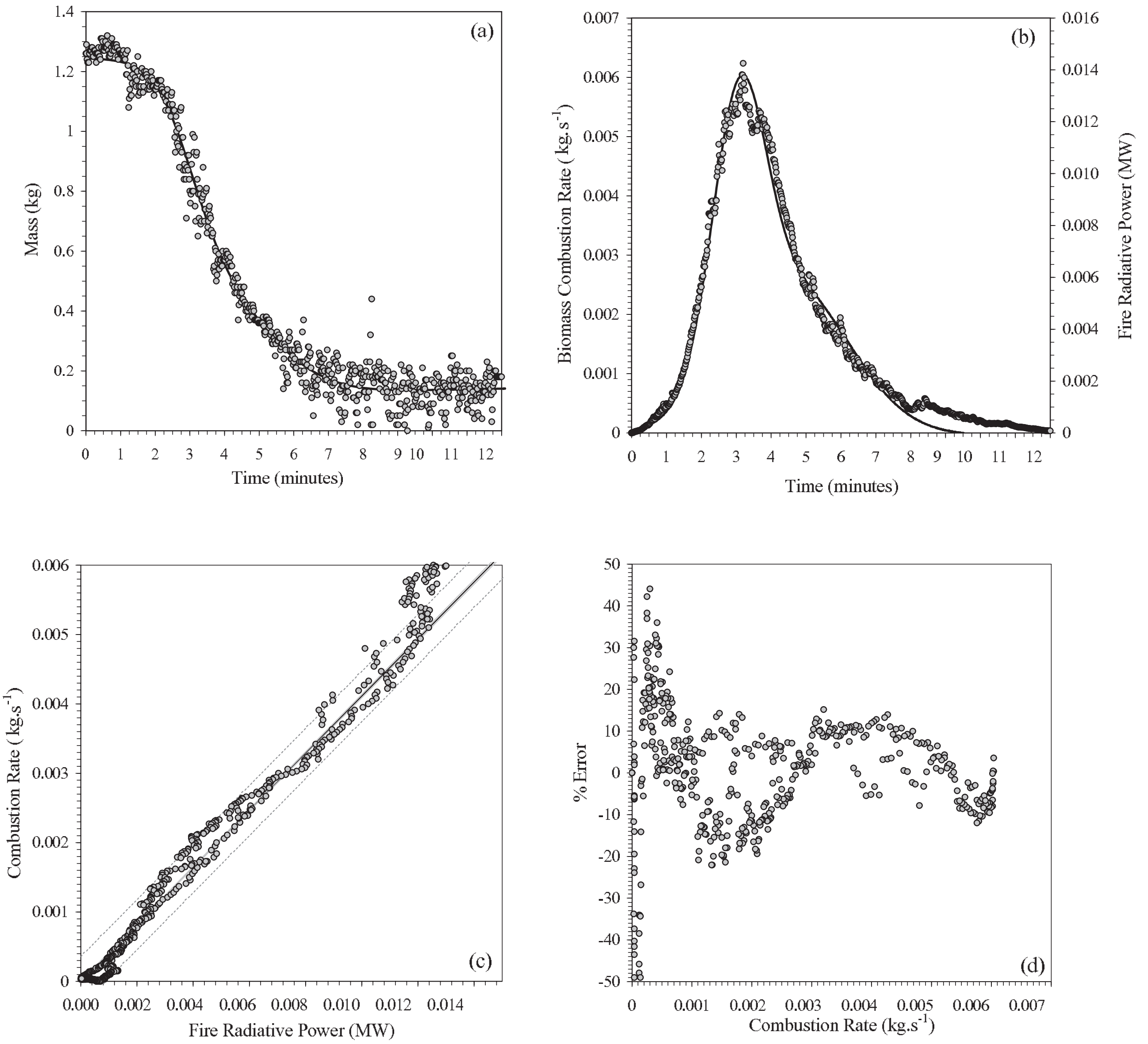

Figure 12. Fire radiative power and fuel consumption for a 1.2 kg *Miscanthus* fire. (a) Fuel mass and best-fit relationship used to calculate biomass combustion rate, (b) biomass combustion rate (line) and fire radiative power (symbols) time-series, (c) scatterplot of fire radiative power against biomass combustion rate including OLS linear best-fit passing through the origin, and (d) percentage residual error on the best-fit relationship shown in Figure 12c, indicating that, in this case FRP could be used to estimate combustion rate to within ±15%, apart from at the lowest rates of combustion where, as can be seen from Figure 12a, the mass data are subject to greatest noise.

and biomass combusted and applying the Mann-Whitney U test to the *Miscanthus* and other fuel type groups indicates that the null hypothesis cannot be rejected at the 95% confidence level, and thus we have no evidence to suppose that the relationship between FRE and biomass combusted is significantly dependent on vegetation type. Therefore, if reliable FRE retrievals can be made via repetitive airborne or spaceborne FRP observations, then without detailed knowledge of the fuel types such data should be able to be converted into fuel consumption estimates using:

$$\text{Fuel biomass combusted(kg)} = 0.368(\pm 0.015).\ \text{FRE(MJ)} \tag{13}$$

At the spatial scales involved when using spaceborne data, a pixel will very likely contain still cooling burned areas immediately behind the active fire font, a space-integrated situation somewhat akin to the time-integrated measure used to derive equation (13). In such situations the combustion rate can therefore perhaps best be derived from the derivative of this relationship with respect to time, since real spaceborne observations will include this energy component along with that from the active fire itself:

$$\text{Rate of biomass combustion}\left(\text{kg.sec}^{-1}\right) = 0.368(\pm 0.015).\ \text{FRP(MW)} \tag{14}$$

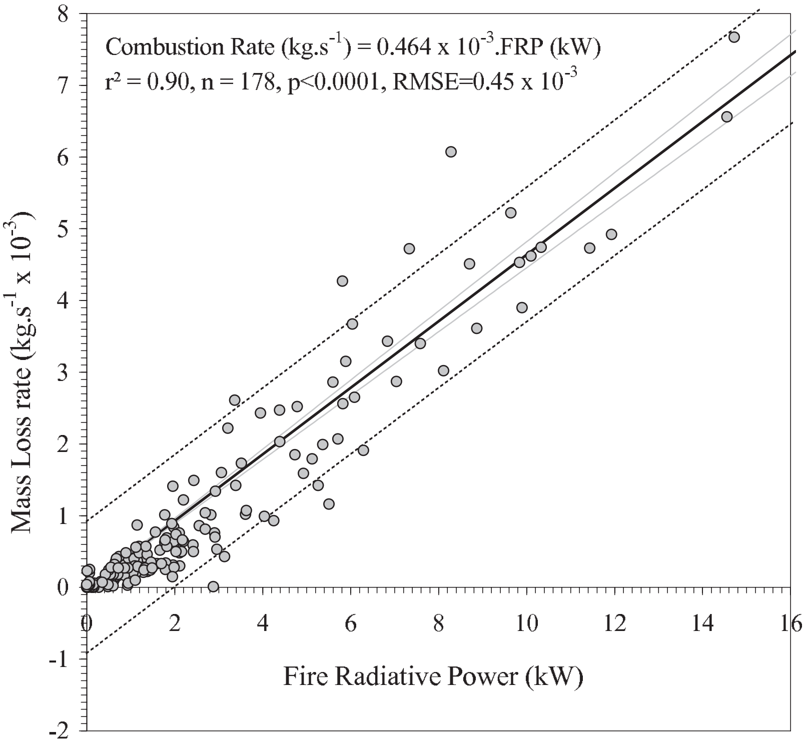

Figure 13. Relationship between biomass combustion rate and fire radiative power calculated from *Miscanthus* fires (in total twenty nine plots of the sort shown in Figure 12c). Source data were subsampled at a three-minute interval to avoid influences from temporal autocorrelation. The OLS linear best-fit passing through the origin (dark line) is shown, along with the 95% confidence intervals on the mean (grey line) and on the prediction (dashed line), the latter having slopes 0.446 and 0.482, respectively.

The difference in the radiative energy combustion factor between equations (12) and (14) is therefore due to additional energy release by the fire after the combustion rate has fallen to zero (e.g., Figure 12a), which is taken into account in the derivation of equation (14) but not (12).

[49] Data from the *Miscanthus*-only fires were used to calculate that 13 ± 3% [mean ± 1 SD] of the total theoretically available maximum heat yield of *Miscanthus* was detected as radiant energy emission, with some indication that the percentage tends to increase with mass combusted (Figure 15). It is known that grassland fires with larger available fuel loads tend to have greater combustion completeness [e.g., *Smith et al.*, 2005] and so release a greater proportion of their total theoretical heat yield. However, since the fuel mass consumed was calculated via differencing of the pre- and post-fire masses, combustion completeness variations are already taken into account. Rather the trend might be related to the fact that the smallest fires were characterised by lower temperatures and small flaming areas, such that a larger proportion of the pixels failed to meet the 477 K detection threshold and/or lay in the region of the Figure 2 or Figure 4 curves where FRP is underestimated by the MIR radiance method.

[50] As a final analysis, video records of each fire were used to divide the combustion regime into smoldering, mixed, and flaming stages where possible (some fires did not exhibit clearly separable stages, or only exhibited a single stage). The percentage of the total fuel biomass combusted during each of these three stages was calculated and compared to the percentage of the total FRE released in the corresponding periods (Figure 16). Interaction terms [*Quinn and Keough*, 2002] indicate that the slopes of the regression lines for the three independent combustion stages differ significantly ($F = 8.1039$, $p < 0.0001$, $df = 2$), and the data suggest that during the smoldering (typically final) stage of each fire there is a tendency for a lower percentage mass loss to occur relative to the percentage of FRE released. Again, this relates to the fact that as smoldering combustion becomes more dominant in a fire, significant residual heat can be radiated from areas of previous combustion that are not now contributing to mass loss.

5.3. Analysis of Competing Heat Loss Mechanisms

[51] The theoretical maximum heat yield of *Miscanthus* is quoted as 17100–19400 kJ.kg^{-1} [*Scurlock*, 1999], yet our experiments indicate a maximum radiative heat yield approaching only 20% of this (Figure 15). *Ferguson et al.* [2000] suggests that between 20 and 60% of the heat liberated in a wildfire is in the form of radiation, with other heat loss mechanisms responsible for the remainder. Due to the outdoor experimental setup, it was not possible to accurately measure convective energy losses. However, conductive losses were estimated using a heat-flux plate buried at three cm depth in the sand underlying the fuel bed. For an example fire, Figure 17 indicates that the maximum rate of radiative heat loss (i.e., FRP) is almost two orders of magnitude greater than the maximum rate of conductive

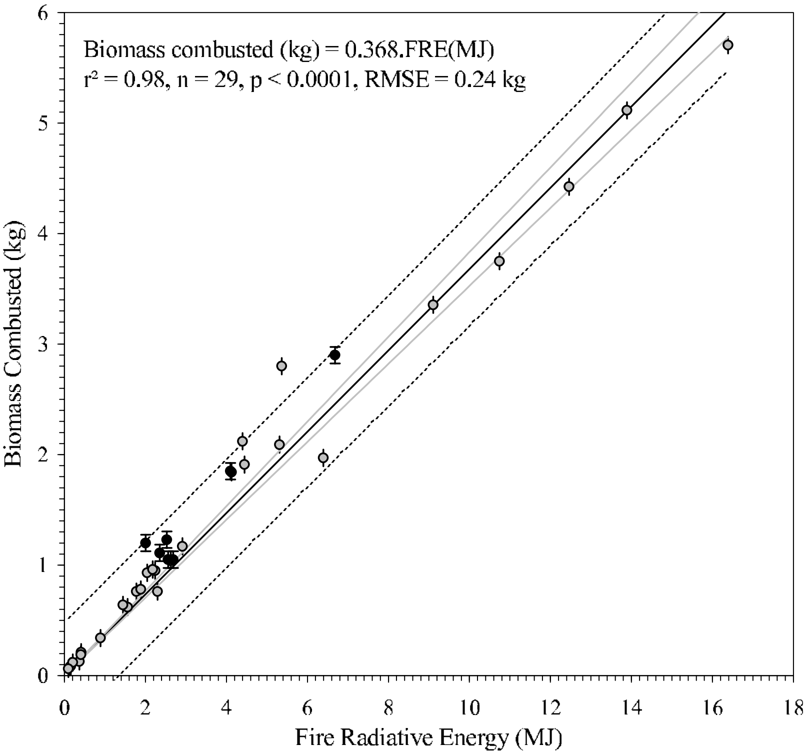

Figure 14. Relationship between fire radiative energy and fuel biomass combusted; error bars are derived from the precision of the digital scales. Grey circles are *Miscanthus* grass, while solid circles are fires of other grasses and woody fuels. For the *Miscanthus* data (29 points) the OLS linear best-fit passing through the origin (dark line) is shown, along with the 95% confidence intervals on the mean (grey line) and on the prediction (dashed line), are shown, the latter having slopes 0.353 and 0.383, respectively.

heat loss. However, radiative losses cease soon after the fire extinguishes, whereas conduction proceeds for a considerably extended period. Thus, the cumulative amount of energy lost by each process is much closer than is the difference in maximum heat loss rates. The total amount of energy lost via conduction is one quarter of that lost via radiation. Nevertheless, this indicates that conduction is clearly not responsible for the large (minimum ∼80%) difference between the theoretical maximum heat yield and the FRE measured in our experiments. Instead, this difference must be explained by: (1) the operation of a substantial convective heat loss mechanism, and perhaps an additional radiative mechanism from the CO_2 emission band that sensing at 3.9 μm fails to detect, (2) the fact that the MIR radiance method does not provide a perfect measure of radiative heat yield (Figures 2 and 4), (3) the radiative emission from the soot particles within a flame will be emitted in all directions rather than just the viewing hemisphere assumed in surface emission calculations, and (4) the true heat yield released in conditions such as those found here maybe somewhat less than that derived via laboratory calorimeter experiments [*Pyne*, 1984].

[52] Nevertheless, what is most important here is that a statistically robust relationship has been derived between remotely sensed fire radiative power and energy measures and the respective rates and totals of fuel biomass combustion. To reliably apply these relationships to MIR remote sensing data from true savanna or forest wildfires, for

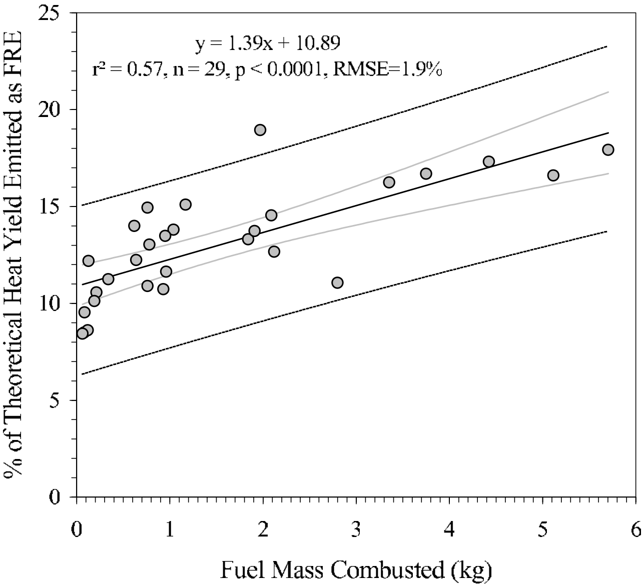

Figure 15. Percentage of the theoretical heat yield released as FRE in the *Miscanthus* fires whose data are shown in Figure 14. The OLS linear best fit is shown, along with 95% confidence intervals on this relationship (grey line) and on the prediction of y from x (dashed line).

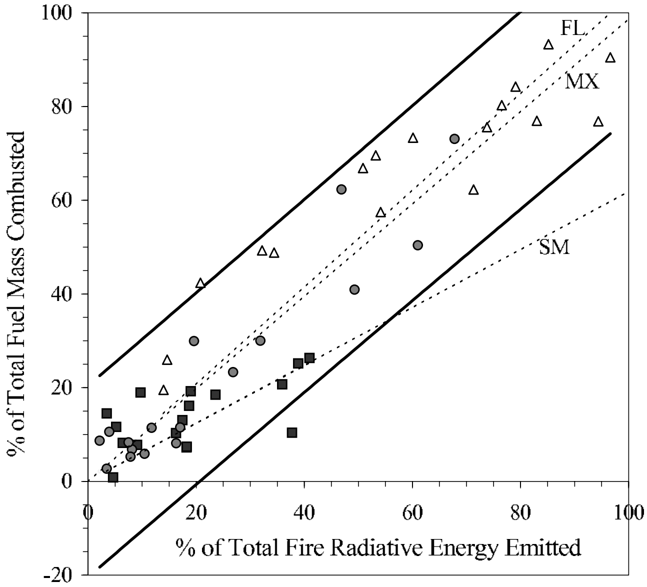

Figure 16. Comparison of the percentage of the total fuel mass combusted in the three stages of the fires [flaming (triangles), mixed (circles), and smoldering (squares)] compared to the percentage of the total fire radiative energy released in each stage. Data for seventeen fires for which discrete combustion stages were identifiable from the video record are shown. Dashed lines (labeled FL, MX, and SM) indicate the OLS linear best-fit passing through the origin for the stages of flaming, mixed and smoldering combustion, respectively. Solid lines indicate the 95% confidence limits on the prediction of %mass combusted from %FRE emitted.

example MIR scenes such as those shown in Figure 1, or MIR-derived FRP time-series such as that shown as Figure 18, requires further testing to ensure that the relationships derived herein are suitable for use in such conditions, and that the FRP and FRE retrieved with such systems are reliable representations of the surface emitted power outputs. The sensitivity analysis undertaken here goes some way to assessing the theoretical accuracy of such observations, while the companion paper by *Roberts et al.* [2005] provides comparisons and validations using data from the SEVIRI sensor onboard the geostationary Meteosat-8 spacecraft. Once confidence has been gained in the combined use of spaceborne FRP data and the FRE emission factors presented here, biomass combustion rates and totals can be derived from high temporal resolution SEVIRI data for the entire African continent. Similarly GOES and MTSAT may provide comparable data over, respectively, the America's and Australasia, though the degree of sensor saturation and nondetection of smaller fires will vary between these systems and eco-regions. Higher spatial resolution data from MODIS will allow the fire radiative power emissions from fires too small to be detected by these geostationary systems also to be considered at least four times per day.

6. Conclusions

[53] The majority of current pyrogenic pollutant emissions estimates are derived via the application of so-called gas and aerosols emission factors to assessments of the amount of dry fuel biomass combusted [*Andreae and Merlet*, 2001]. However, such fuel combustion estimates have often proved difficult to quantify remotely, usually relying on the combination of remotely sensed burned area

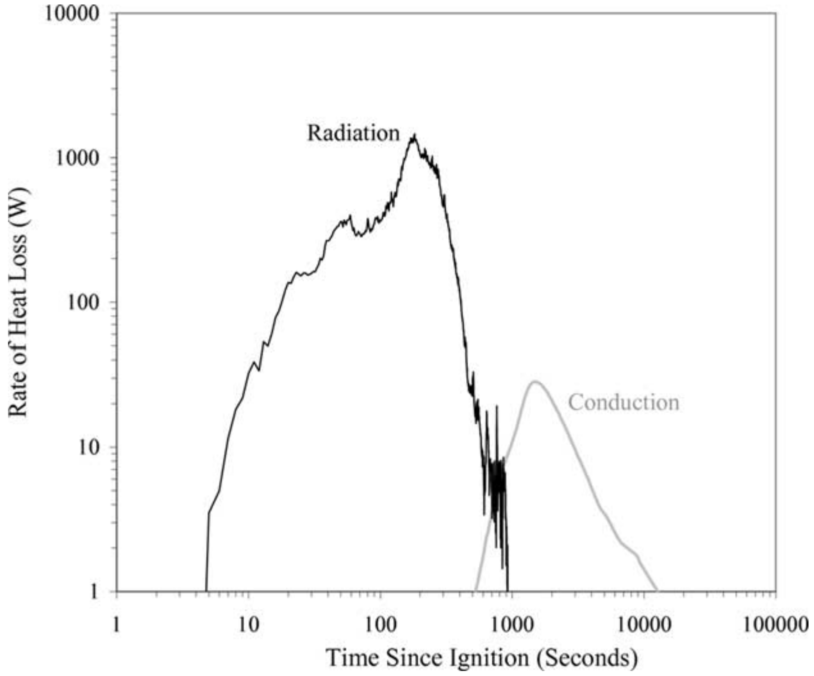

Figure 17. Comparison of heat loss rates due to radiation (calculated via Fire Radiative Power) and conduction (calculated via soil heat flux plate buried 3 cm below fire). Fuel was 0.2 kg *Miscanthus*. Total energy lost via radiation is estimated to be 240 kJ, while via conduction is 57 kJ.

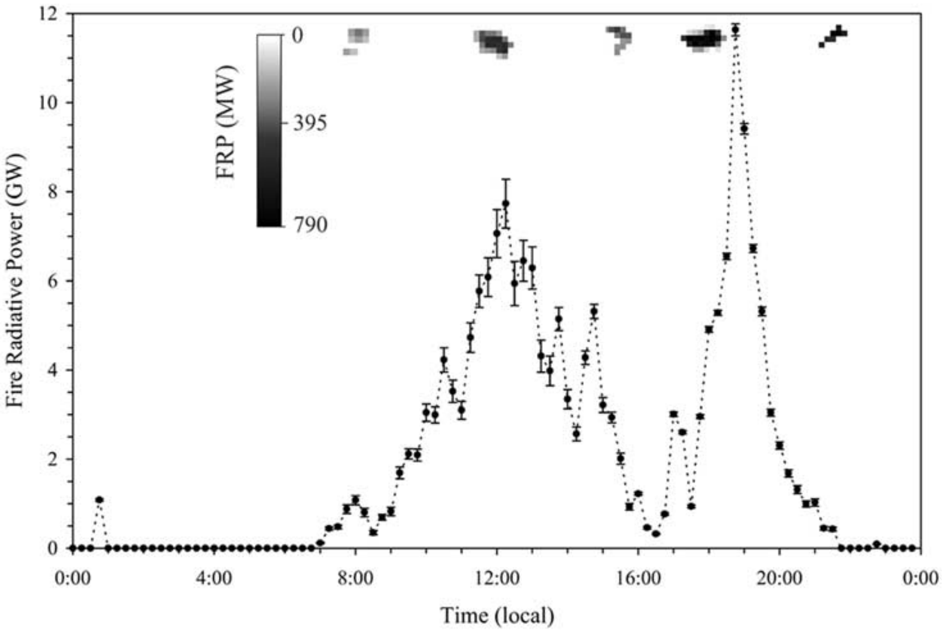

Figure 18. Fire Radiative Power (FRP) time series of a savanna fire burning in northern Botswana on 4 September 2003, calculated from 15-minute temporal resolution Meteosat-8 SEVIRI imagery. For each image, the FRP value in Wm^{-2} resulting from application of equations (5) and (10) to each detected fire pixel is converted to a total GWatt value for the whole fire via summation over all active fire pixels, multiplication by the SEVIRI pixel area at the fires geographic location, and correction for the oversampling factor (SEVIRI pixels have a nominal FOV of 4.8 km and are spaced 3 km apart at the subsatellite point). Error bars denote the uncertainty in derived FRP, calculated by taking into account uncertainty in the fire pixel background signal ($\Delta L_{b,MIR}$) as expressed by the standard deviation of the surrounding nonfire pixel signals. Uncertainties for each pixel contributing to the overall active fire cluster FRP measure are summed to create the overall error bar at each time step, so this generally increases in magnitude with the number of fire pixels within the cluster. Uncertainties decrease toward the evening when ambient background pixel signal variations are lower. Illustrated at top are maps of active fire pixel FRP, indicating its spatio-temporal evolution between 7:12 and 21:12 hours local time. See the companion paper by *Roberts et al.* [2005] for full details of the accuracy and precision of SEVIRI-derived FRP.

measures with estimates of fuel density and combustion completeness that are hard to come by, certainly in terms of near real-time applications. The ability of new remote sensing systems to directly estimate the rate of emission of fire radiative energy in large-scale natural wildfires opens the way for the direct estimation of fuel consumption rates and totals via quantification of the fire radiative power output, and its conversion to combustion measures via application of a so-called radiative energy combustion factor. We have presented the results of small-scale experiments designed to validate the retrieval of FRP using a single waveband (MIR radiance) algorithm akin to that applied to spaceborne sensor data, and have analysed the sensitivity of this method to assumptions made during the algorithm derivation and to inaccuracies in its parameterisation. We have shown the MIR radiance method to be insensitive to assumptions made during the algorithm derivation, and have shown it to be a robust method of estimating FRP provided it is well parameterised. The methods potential disadvantage is that it significantly underestimates radiative emissions from components of the fire significantly cooler than ~650 K, though these are in any case of low intensity compared to the hotter parts of the fire and the propensity to underestimate their contribution may in fact in some cases be considered advantageous since they are likely to be cooling post-fire areas (rather than areas of active combustion) and thus will not be contributing to the actual combustion rate. A major advantage of the MIR radiance method that it is relatively insensitive to inaccuracies in the assumed background radiance of the fire pixel, much more so that the bi-spectral method of *Dozier* [1981], where the relatively weak fire signal in the TIR channel causes far greater sensitivity to such error. For example, results from *Wooster et al.* [2003, Figure 8c] indicate that application of the *Dozier* [1981] method to an 800 K fire of fractional area 0.001 where the assumed background signal is underestimated by the equivalent of 5 K leads to a factor of two (i.e., 100%) overestimate in FRP. Figure 5 indicates that for the same fire and background signal underestimate (equivalent to $\Delta L_{b,MIR} = 0.124\ Wm^{-2}\ sr^{-1}\ \mu m^{-1}$) the FRP is overestimated by only 18% via the MIR radiance method.

[54] The FRE method in theory removes the requirement for fuel density or combustion completeness measures when deriving estimates of wildfire fuel consumption, and the (admittedly limited) set of fuels thus far tested suggests that detailed knowledge of the fuel type may be relatively

unnecessary. However, we find that only 13 ± 3% [mean ± 1SD] of the theoretically available heat of the fuel is detected as FRE by our nadir-viewing MIR imaging system, which agrees with recent work illustrating the use of MODIS FRP data to derive 'radiative' savannah fireline intensity measures whose values were around an order of magnitude lower than those of traditional FLI measures calculated from the theoretical fuel heat yield and in situ measurements of fuel consumption and fire rate of spread [*Smith and Wooster*, 2005]. We therefore conclude that the majority of fuel energy in both our experimental fires and in the sorts of natural savannah fires observable from MODIS is liberated via other heat loss mechanisms, most notably convection, and thus the ability to reliably use the FRE combustion factor to convert between measures of radiative energy and biomass combustion will depend on the extent to which the partitioning of the total energy release into radiative, convective and other heat loss mechanisms remains independent of the fire and fuel characteristics. This is as yet unknown, but there may be some dependence of this partitioning on the specific behaviour of the fuel and/or the depth, size and temperature of the fire. Nevertheless, we find that for experimental *Miscanthus* fires whose fuel loadings varied by almost two orders of magnitude, the linear relationship between fuel consumption and FRE emission is extremely statistically significant ($r^2 = 0.98$, $n = 29$, $p < 0.0001$). Therefore, while keeping in mind the above provisos, and the fact that the methods used to estimate FRP from spaceborne data all have a certain degree of measurement uncertainty involved (as discussed herein and in *Wooster et al.* [2003] and *Zhukov et al.* [2005b]), once fully validated the FRE combustion factor presented here can be used with satellite-derived FRP observations to derive new insights into fuel consumption rates in large-scale natural fires, and when integrated over time can provide a new, more direct method of estimating amounts of fuel biomass combusted from which estimates of the release of pyrogenic aerosol and trace gases maybe derived.

[55] **Acknowledgments.** This study was supported by NERC New Observing Techniques (NOT) grant NER/Z/S/2001/01027. SEVIRI data were kindly provided under an ESA/EUMETSAT AO, BIRD data from DLR and MODIS data from the NASA Goddard Space Flight Center (GSFC) and EROS Data Centre DAACs. GOES data are courtesy of NOAA/NESDIS. The authors would like to thank IACR-Rothamsted, and in particular the staff of Rothamsted Experimental Farm, for their unswerving support during the field component of this research. We would also like to thank the various staff and students of the Department of Geography, King's College London, who graciously assisted us in the fieldwork. We are extremely grateful to the staff of the NERC/EPFS equipment pool at the University of Southampton for their training and loan of the GER-3700 spectroradiometer and in their efforts to develop a robust calibration procedure suitable for use with active fire observations. Our thanks go to the anonymous reviewers who suggested useful and important clarifications to the content of this manuscript.

References

Alexander, M. E. (1982), Calculating and interpreting forest fire intensities, *Can. J. Bot.*, *60*, 349–357.

Anderson, G. P., et al. (1995), History of one family of atmospheric radiative transfer codes, in *Passive Infrared Remote Sensing of Clouds and the Atmosphere II*, edited by D. K. Lynch, *SPIE, 2309*, 170–183.

Andreae, M. O. (1991), Biomass burning: Its history, use and distribution and its impact on the environmental quality and global climate, in *Global Biomass Burning: Atmospheric, Climatic and Biospheric Implications*, edited by J. S. Levine, pp. 2–21, MIT Press, Cambridge, Mass.

Andreae, M. O., and P. Merlet (2001), Emission of trace gases and aerosols from biomass burning, *Global Biogeochem. Cycles*, *15*, 955–966.

Barbosa, P., D. Stroppiana, J. Gregoir, and J. Pereira (1999), An assessment of vegetation fire activity in Africa (1981–1991): Burned areas, burned biomass, and atmospheric emissions, *Global Biogeochem. Cycles*, *13*, 933–950.

Borrell, P., J. P. Burrows, U. Platt, and C. Zehner (2001), Determining tropospheric concentrations of trace gases from space, *ESA Bull.*, *107*, 72–81.

Borrell, P., J. P. Burrows, U. Platt, A. Richter, and T. Wagner (2003), New directions: New developments in satellite capabilities for probing the chemistry of the troposphere, *Atmos. Environ.*, *37*, 2567–2570.

Byram, G. M. (1959), Combustion of forest fuels, in *Forest Fire: Control and Use*, edited by K. P. Brown, pp. 65–89, McGraw-Hill, New York.

Chou, M. D., P. K. Chan, and M. H. Wang (2002), Aerosol radiative forcing derived from SeaWiFS-retrieved aerosol optical properties, *J. Atmos. Sci.*, *59*, 748–757.

Dozier, J. (1981), A method for satellite identification of surface temperature fields of subpixel resolution, *Remote Sens. Environ.*, *11*, 221–229.

Ferguson, S., D. Sandberg, and R. Ottmar (2000), Modelling the effect of land use changes on global biomass emissions, in *Biomass Burning and Its Inter-relationship With the Climate System*, edited by J. L. Innes, M. Beniston, and M. M. Verstraete, pp. 33–50, Springer, New York.

Flynn, L. P., P. J. Mouginis-Mark, J. C. Gradie, and P. Lucey (1993), Radiative temperature measurements at Kupaianaha lava lake, Kilauea Volcano, Hawaii, *J. Geophys. Res.*, *98*, 6461–6476.

French, N. H., P. Goovaerts, and E. S. Kasischke (2004), Uncertainty in estimating carbon emissions from boreal forest fires, *J. Geophys. Res.*, *109*, D14S08, doi:10.1029/2003JD003635.

Gaydon, A. G., and H. G. Wolfhard (1970), *Flames: Their Structure, Radiation and Temperature*, 3rd ed., CRC Press, Boca Raton, Fla.

Giglio, L., and C. O. Justice (2003), Effect of wavelength selection on characterisation of fire size and temperature, *Int. J. Remote Sens.*, *24*, 3515–3520.

Giglio, L., and J. D. Kendall (2001), Application of the Dozier retrieval to wildfire characterisation: A sensitivity analysis, *Remote Sens. Environ.*, *77*, 34–49.

Giglio, L., J. Descloitres, C. Justice, and Y. Kaufman (2003), An enhanced contextual fire detection algorithm for MODIS, *Remote Sens. Environ.*, *87*, 273–282.

GTOS (2000), IGOS-P carbon cycle observation theme: Terrestrial and atmospheric components, *GTOS-25*, 50 pp.

Ito, A., and J. E. Penner (2004), Global estimates of biomass burning emissions based on satellite imagery for the year 2000, *J. Geophys. Res.*, *109*, D14S05, doi:10.1029/2003JD004423.

Justice, C. O., L. Giglio, S. Korontzi, J. Owens, J. T. Morisette, D. Roy, J. Descloitres, S. Alleaume, F. Petitcolin, and Y. Kaufman (2002), The MODIS fire products, *Remote Sens. Environ.*, *83*, 244–262.

Kaufman, Y., L. Remer, R. Ottmar, D. Ward, L. Rong, R. Kleidman, R. Fraser, L. Flynn, D. McDougal, and G. Shelton (1996), Relationship between remotely sensed fire intensity and rate of emission of smoke: SCAR-C experiment, in *Global Biomass Burning*, edited by J. Levine, pp. 685–696, MIT Press, Cambridge, Mass.

Kaufman, Y. J., C. Justice, L. Flynn, J. Kandall, E. Prins, D. E. Ward, P. Menzel, and A. Setzer (1998a), Monitoring global fires from EOS-MODIS, *J. Geophys. Res.*, *103*, 32,215–32,239.

Kaufman, Y. J., R. G. Kleidman, and M. D. King (1998b), SCAR-B fires in the tropics: Properties and their remote sensing from EOS-MODIS, *J. Geophys. Res.*, *103*, 31,955–31,969.

Kaufman, Y. J., D. Tanré, and O. Boucher (2002), A satellite view of aerosols in the climate system, *Nature*, *419*, 215–223.

King, M. D., Y. J. Kaufman, D. Tanré, and T. Nakajima (1999), Remote sensing of tropospheric aerosols from space: Past, present, and future, *Bull. Am. Meteorol. Soc.*, *80*, 2229–2259.

Korontzi, S., D. P. Roy, C. O. Justice, and D. E. Ward (2004), Modeling and sensitivity analysis of fire emissions in southern Africa during SAFARI 2000, *Remote Sens. Environ.*, *92*, 255–275.

Langaas, S. (1993), A parametrised bispectral model for savanna fire detection using AVHRR night images, *Int. J. Remote Sens.*, *14*, 2245–2262.

Langaas, S. (1995), A critical review of sub-resolution fire detection techniques and principles using thermal satellite data, Ph.D. thesis, Dep. of Geogr., Univ. of Oslo, Oslo, Norway.

Lobert, J. M., and J. Warnatz (1993), Emissions from the combustion process in vegetation, in *Fire in the Environment: The Ecological, Atmospheric and Climatic Importance of Vegetation Fires*, edited by P. J. Crutzen and J. G. Goldammer, pp. 15–39, John Wiley, Hoboken, N. J.

McNaughton, S. J., N. R. H. Stronach, and N. J. Georgiadis (1998), Combustion in natural fires and global emissions budgets, *Ecol. Appl.*, *8*, 464–468.

Menzel, W. P., and E. M. Prins (1996), Monitoring biomass burning with the new generation of geostationary satellites, in *Biomass Burning and Global Change: Remote Sensing, Modeling, and Inventory Development, and Biomass Burning in Africa*, vol. 1, edited by J. S. Levine, pp. 56–64, MIT Press, Cambridge, Mass.

Oertel, K., et al. (2003), Airborne forest fire mapping with an adaptive infrared sensor, *Int. J. Remote Sens.*, *24*, 3663–3682.

Ohlemiller, T. J. (1995), Smoldering combustion, in *SFPE Handbook of Fire Protection Engineering*, 2nd ed., vol. 2, edited by M. A. Quincy et al., pp. 171–179, Building and Fire Res. Lab., Natl. Inst. of Stand., Gaithersburg, Md.

Prins, E. M., and W. P. Menzel (1994), Trends in South American biomass burning with the GOES visible infrared spin scan radiometer atmospheric sounder from 1983 to 1991, *J. Geophys. Res.*, *99*, 16,719–16,735.

Prins, E. M., J. M. Felts, W. P. Menzel, and D. E. Ward (1998), An overview of GOES-8 diurnal fire and smoke results for SCAR-B and 1995 fire season in South America, *J. Geophys. Res.*, *103*, 31,821–31,835.

Pyne, S. J. (1984), *Introduction to Wildland Fire: Fire Management in the United States*, John Wiley, Hoboken, N. J.

Quinn, G. P., and M. J. Keough (2002), *Experimental Design and Data Analysis for Biologists*, Cambridge Univ. Press, New York.

Riggan, P., R. Tissell, R. Lockwood, J. Brass, J. Pereira, H. Miranda, T. Campos, and R. Higgins (2004), Remote measurement of energy and carbon flux from wildfires in Brazil, *Ecol. Appl.*, *14*, 855–872.

Roberts, G., M. J. Wooster, G. L. W. Perry, N. A. Drake, L.-M. Rebelo, and F. M. Dipotso (2005), Retrieval of biomass combustion rates and totals from fire radiative power observations: Application to southern Africa using geostationary SEVIRI imagery, *J. Geophys. Res.*, *110*, D21111, doi:10.1029/2005JD006018.

Robinson, J. (1991), Fire from space: Global fire evaluation using infrared remote sensing, *Int. J. Remote Sens.*, *12*, 3–24.

Rosenfeld, D. (1999), TRMM observed first direct evidence of smoke from forest fires inhibiting rainfall, *Geophys. Res. Lett.*, *26*, 3105–3108.

Rothermel, R. C., R. A. Wilson, G. A. Morris, and S. S. Sackett (1986), Modeling moisture content of fine dead wildland fuels input into the BEHAVE fire prediction system, *Res. Pap. INT-359*, U.S. Dep. of Agric. For. Serv., Ogden, Utah.

Roy, D., P. E. Lewis, and C. O. Justice (2002), Burned area mapping using multi-temporal moderate spatial resolutio data—A bi-directional reflectance model-based expectation approach, *Remote Sens. Environ.*, *83*, 263–286.

Schaepman, M. E. (1998), Calibration of a field spectroradiometer, *Remote Sens. Ser. Pap. 31*, 163 pp., Remote Sens. Lab., Dep. of Geogr., Univ. of Zurich, Zurich, Switzerland.

Scholes, M., and M. O. Andreae (2000), Biogenic and pyrogenic emissions from Africa and their impact on the global atmosphere, *Ambio*, *29*, 23–29.

Scholes, R. J., J. Kendal, and C. O. Justice (1996), The quantity of biomass burned in southern Africa, *J. Geophys. Res.*, *101*, 23,667–23,676.

Scurlock, J. M. O. (1999), *Miscanthus*: A review of European experience with a novel energy crop, *Rep. ORNL/TM-13732*, 28 pp., Environ. Sci. Div., Oak Ridge Natl. Lab., Oak Ridge, Tenn.

Seiler, W., and P. J. Crutzen (1980), Estimates of gross and net fluxes of carbon between the biosphere and the atmosphere from biomass burning, *Clim. Change*, *2*, 207–247.

Smith, A. M. S., and M. J. Wooster (2005), Remote classification of head and backfire types from MODIS fire radiative power observations, *Int. J. Wildland Fire*, *14*, 249–254.

Smith, A. M. S., M. J. Wooster, N. A. Drake, F. M. Dipotso, and G. L. W. Perry (2005), Fire in African savanna: Testing the impact of incomplete combustion on pyrogenic emissions estimates, *Ecol. Appl.*, *15*, 1074–1082.

Stroppiana, D., J.-M. Gregoire, and J. M. C. Pereira (2003), The use of SPOT VEGETATION data in a classification tree approach for burnt area mapping in Australian savanna, *Int. J. Remote Sens.*, *24*, 2131–2151.

Trollope, W. S. W., L. A. Trollope, A. L. F. Potgieter, and N. Zambatis (1996), SAFARI-92 characterization of biomass and fire behavior in the small experimental burns in Kruger National Park, *J. Geophys. Res.*, *101*, 23,531–23,540.

Whelan, R. J. (1995), *The Ecology of Fire*, Cambridge Univ. Press, New York.

Wooster, M. J. (2002), Small-scale experimental testing of fire radiative energy for quantifying mass combusted in natural vegetation fires, *Geophys. Res. Lett.*, *29*(21), 2027, doi:10.1029/2002GL015487.

Wooster, M. J., and Y.-H. Zhang (2004), Boreal forest fires burn less intensely in Russia than in North America, *Geophys. Res. Lett.*, *31*, L20505, doi:10.1029/2004GL020805.

Wooster, M. J., B. Zhukov, and D. Oertel (2003), Fire radiative energy for quantitative study of biomass burning: Derivation from the BIRD experimental satellite and comparison to MODIS fire products, *Remote Sens. Environ.*, *86*, 83–107.

Wooster, M. J., G. Perry, B. Zhukov, and D. Oertel (2004), Biomass burning emissions inventories: Modelling and remote sensing of fire intensity and biomass combustion rates, in *Spatial Modelling of the Terrestrial Environment*, edited by R. Kelly, N. Drake, and S. Barr, pp. 175–196, John Wiley, Hoboken, N. J.

Zhang, Y.-H., M. J. Wooster, O. Tutubalina, and G. L. W. Perry (2003), Monthly burned area and forest fire carbon emission estimates for the Russian Federation from SPOT VGT, *Remote Sens. Environ.*, *87*, 1–15.

Zhukov, B., K. Briess, E. Lorenz, D. Oertel, and W. Skrbek (2005a), Detection and analysis of high-temperature events in the BIRD mission, *Acta Astronaut.*, *56*, 65–71.

Zhukov, B., E. Lorenz, D. Oertel, M. J. Wooster, and G. Roberts (2005b), Spaceborne detection and characterization of fires during the Bi-spectral Infrared Detection (BIRD) experimental small satellite mission (2001–2004), *Remote Sens. Environ.*, in press.

Y. J. Kaufman, Laboratory for Atmospheres (913), NASA Goddard Space Flight Center, Greenbelt, MD 20771, USA.

G. L. W. Perry, G. Roberts, and M. J. Wooster, Department of Geography, King's College London, Strand, London WC2R 2LS, UK. (martin.wooster@kcl.ac.uk)